



HAL
open science

CLASSY V: The Impact of Aperture Effects on the Inferred Nebular Properties of Local Star-forming Galaxies

Karla Z. Arellano-Córdova, Matilde Mingozzi, Danielle A. Berg, Bethan L. James, Noah S. J. Rogers, Alessandra Aloisi, Ricardo O. Amorín, Jarle Brinchmann, Stéphane Charlot, John Chisholm, et al.

► **To cite this version:**

Karla Z. Arellano-Córdova, Matilde Mingozzi, Danielle A. Berg, Bethan L. James, Noah S. J. Rogers, et al.. CLASSY V: The Impact of Aperture Effects on the Inferred Nebular Properties of Local Star-forming Galaxies. *The Astrophysical Journal*, 2022, 935, 10.3847/1538-4357/ac7854 . insu-03839657

HAL Id: insu-03839657

<https://insu.hal.science/insu-03839657>

Submitted on 4 Nov 2022

HAL is a multi-disciplinary open access archive for the deposit and dissemination of scientific research documents, whether they are published or not. The documents may come from teaching and research institutions in France or abroad, or from public or private research centers.

L'archive ouverte pluridisciplinaire **HAL**, est destinée au dépôt et à la diffusion de documents scientifiques de niveau recherche, publiés ou non, émanant des établissements d'enseignement et de recherche français ou étrangers, des laboratoires publics ou privés.



Distributed under a Creative Commons Attribution 4.0 International License



CLASSY V: The Impact of Aperture Effects on the Inferred Nebular Properties of Local Star-forming Galaxies

Karla Z. Arellano-Córdova¹, Matilde Mingozi², Danielle A. Berg¹, Bethan L. James³, Noah S. J. Rogers⁴,
Alessandra Aloisi², Ricardo O. Amorín^{5,6}, Jarle Brinchmann⁷, Stéphane Charlot⁸, John Chisholm¹, Timothy Heckman⁹,
Stefany Fabian Dubón¹⁰, Matthew Hayes¹¹, Svea Hernandez³, Tucker Jones¹², Nimisha Kumari³, Claus Leitherer²,
Crystal L. Martin¹³, Themiya Nanayakkara¹⁴, Richard W. Pogge¹⁵, Ryan Sanders¹², Peter Senchyna¹⁶,
Evan D. Skillman¹⁷, Dan P. Stark¹⁸, Aida Wofford¹⁹, and Xinfeng Xu⁹

¹ Department of Astronomy, The University of Texas at Austin, 2515 Speedway, Stop C1400, Austin, TX 78712, USA; kzarellano@utexas.edu

² Space Telescope Science Institute, 3700 San Martin Drive, Baltimore, MD 21218, USA

³ AURA for ESA, Space Telescope Science Institute, 3700 San Martin Drive, Baltimore, MD 21218, USA

⁴ Minnesota Institute for Astrophysics, University of Minnesota, 116 Church Street SE, Minneapolis, MN 55455, USA

⁵ Instituto de Investigación Multidisciplinar en Ciencia y Tecnología, Universidad de La Serena, Raul Bitrán 1305, La Serena 2204000, Chile

⁶ Departamento de Astronomía, Universidad de La Serena, Avenida Juan Cisternas 1200 Norte, La Serena 1720236, Chile

⁷ Instituto de Astrofísica e Ciências do Espaço, Universidade do Porto, CAUP, Rua das Estrelas, PT4150-762 Porto, Portugal

⁸ Sorbonne Université, CNRS, UMR7095, Institut d'Astrophysique de Paris, F-75014, Paris, France

⁹ Center for Astrophysical Sciences, Department of Physics & Astronomy, Johns Hopkins University, Baltimore, MD 21218, USA

¹⁰ Department of Physics, Bryn Mawr College, Bryn Mawr, PA 19010, USA

¹¹ Stockholm University, Department of Astronomy and Oskar Klein Centre for Cosmoparticle Physics, AlbaNova University Centre, SE-10691, Stockholm, Sweden

¹² Department of Physics and Astronomy, University of California, One Shields Avenue, Davis, CA 95616, USA

¹³ Department of Physics, University of California, Santa Barbara, Santa Barbara, CA 93106, USA

¹⁴ Centre for Astrophysics and Supercomputing, Swinburne University of Technology, Hawthorn, VIC 3122, Australia

¹⁵ Department of Astronomy, The Ohio State University, 140 W 18th Avenue, Columbus, OH 43210, USA

¹⁶ Carnegie Observatories, 813 Santa Barbara Street, Pasadena, CA 91101, USA

¹⁷ Minnesota Institute for Astrophysics, University of Minnesota, 116 Church Street SE, Minneapolis, MN 55455, USA

¹⁸ Steward Observatory, The University of Arizona, 933 N Cherry Avenue, Tucson, AZ, 85721, USA

¹⁹ Instituto de Astronomía, Universidad Nacional Autónoma de México, Unidad Académica en Ensenada, Km 103 Carr. Tijuana-Ensenada, Ensenada 22860, México

Received 2022 April 18; revised 2022 June 1; accepted 2022 June 8; published 2022 August 17

Abstract

Strong nebular emission lines are an important diagnostic tool for tracing the evolution of star-forming galaxies across cosmic time. However, different observational setups can affect these lines, and the derivation of the physical nebular properties. We analyze 12 local star-forming galaxies from the COS Legacy Spectroscopy SurveyY (CLASSY) to assess the impact of using different aperture combinations on the determination of the physical conditions and gas-phase metallicity. We compare optical spectra observed with the Sloan Digital Sky Survey Data Release aperture, which has a 3" diameter similar to COS, IFU, and long-slit spectra, including new LBT/MODS observations of five CLASSY galaxies. We calculate the reddening, electron densities and temperatures, metallicities, star formation rates, and equivalent widths (EWs). We find that measurements of the electron densities and temperatures, and metallicity remained roughly constant with aperture size, indicating that the gas conditions are relatively uniform for this sample. However, using IFU observations of three galaxies, we find that the $E(B - V)$ values derived from the Balmer ratios decrease (by up to 53%) with increasing aperture size. The values change most significantly in the center of the galaxies, and level out near the COS aperture diameter of 2".5. We examine the relative contributions from the gas and stars using the $H\alpha$ and $[O III] \lambda 5007$ EWs as a function of aperture light fraction, but find little to no variations within a given galaxy. These results imply that the optical spectra provide nebular properties appropriate for the far-UV CLASSY spectra, even when narrow 1"0 long-slit observations are used.

Unified Astronomy Thesaurus concepts: [Emission line galaxies \(459\)](#); [Optical astronomy \(1776\)](#); [Galaxy abundances \(574\)](#); [Dwarf galaxies \(416\)](#)

1. Introduction

A key goal of galaxy evolution is to understand the main processes shaping the stellar and nebular gas content of galaxies across cosmic time. In the coming years, the new generation of space and ground-based telescopes, such as the James Webb Space Telescope (JWST) and the Extremely Large Telescopes (ELTs) will provide the first probes of the physical

conditions in the first galaxies. In this context, the study of nearby, chemically young, high-ionization dwarf galaxies provides a more detailed view of conditions similar to these high- z systems (e.g., Senchyna et al. 2017, 2019; Berg et al. 2021), and thus, helps constrain and interpret their physical properties. In particular, optical emission spectra of local, star-forming, dwarf galaxies provide a rich source of information about the physical properties of their interstellar medium (ISM), such as dust content, electron density and temperature structure, gas-phase metallicity, and the ionization state of the gas (e.g., Lequeux et al. 1979; Campbell et al. 1986; Skillman et al. 1989; Pagel et al. 1992; Vilchez 1995; Izotov &

Thuan 1999; Kunth & Östlin 2000; Berg et al. 2012, 2016; Sánchez Almeida et al. 2016; Guseva et al. 2017; James et al. 2017; Berg et al. 2019; McQuinn et al. 2020, and many more).

Recently, Berg et al. (2022; hereafter, Paper I) presented the COS Legacy Archive Spectroscopic SurveY (CLASSY) treasury, obtained with Cosmic Origins Spectrograph (COS) on board the Hubble Space Telescope (HST). CLASSY comprises a sample of 45 local ($0.002 < z < 0.182$) star-forming galaxies with high-resolution ($R \sim 15,000$) far-ultraviolet (FUV) COS spectra and moderate-resolution ($R \sim 2000$) optical spectra. Most of the optical observations are archival spectra from the Sloan Digital Sky Survey Data Release 12 (SDSS; Eisenstein et al. 2011), but are complemented by long-slit and integral field unit spectroscopy (IFU) spectroscopy for some CLASSY galaxies (e.g., ESO 096.B-0923; PI: Östlin, ESO 0103.B-0531; PI: Erb; Senchyna et al. 2019; R. L. Sanders et al. in preparation). The CLASSY sample covers a broad range of physical properties such as reddening ($0.02 < E(B - V) < 0.67$), nebular density, ($10 < n_e$ (cm^{-3}) < 1120), gas-phase metallicity ($7.0 < 12 + \log(\text{O}/\text{H}) < 8.7$), ionization parameter ($0.5 < [\text{O III}] \lambda 5007 / [\text{O II}] \lambda 3727 < 38.0$), stellar mass ($6.2 < \log M_* (M_\odot) < 10.1$), and star formation rate (SFR) ($-2.0 < \log \text{SFR} (M_\odot \text{yr}^{-1}) < +1.6$). One of the main purposes of CLASSY is to create a database of local star-forming galaxies to study and interpret the physical properties of the stellar and gas-phase content of star-forming galaxies across all redshifts. However, in contrast to distant galaxies, a large fraction of the light of these very nearby objects can fall out of the aperture of the fiber or slit used, resulting in aperture effect issues.

While optical spectra of individual H II regions in nearby galaxies have provided the foundation for diagnosing the physical conditions in nebular gas, it is not yet clear whether the same diagnostics are appropriate for the integrated-light spectra observed from distant galaxies (e.g., Kobulnicky & Kennicutt 1999; Moustakas & Kennicutt 2006). Several studies have focused their attention on the combined impact of aperture size with different galaxy morphologies on the inferred physical properties of local and high-redshift galaxies (e.g., Zaritsky et al. 1995; Pérez-González et al. 2003; Gómez et al. 2003; Hopkins et al. 2003; Brinchmann et al. 2004; Kewley et al. 2005). For example, Kewley et al. (2005) presented an analysis of the aperture effects on the computation of SFR, reddening ($E(B - V)$), and gas-phase metallicity for different Hubble-type galaxies. These authors concluded that apertures capturing $< 20\%$ of the total galaxy’s light show significant differences in the determination of the global galaxy properties. Therefore, aperture effects can strongly bias comparisons among different surveys (Kewley et al. 2005). As such, aperture corrections are fundamental for small apertures to avoid biases (Hopkins et al. 2003; Nakamura et al. 2004; Brinchmann et al. 2004).

Recently, Mannucci et al. (2021) analyzed the impact of the different aperture sizes (e.g., representative apertures for long-slit and IFU spectroscopy) from parsec to kiloparsec scales in nearby galaxies. These authors found significant differences in the flux ratios involving low-ionization emission lines (i.e., $[\text{S II}] \lambda\lambda 6717, 6731 / \text{H}\beta$) mainly due to the internal structure of the H II regions. While we cannot resolve individual H II regions in most dwarf star-forming galaxies, aperture effects may still play an important role when different instruments/apertures sampling different physical sizes of the same galaxy.

Therefore, aperture effects can lead to significant biases that affect the computation of the physical properties in both local star-forming galaxies and high-redshift galaxies (Kewley et al. 2005; Pérez-González et al. 2003; Gómez et al. 2003; Brinchmann et al. 2004). For this reason, it is important to understand and characterize the effects of aperture size on the interpretation of galaxy properties derived from rest-frame optical spectra.

In this paper, we present an analysis of the 12 CLASSY galaxies for which multiple optical spectra exist with different apertures. The variations in spatial scales probed by these different spectra provide an ideal laboratory to assess the variations of physical properties. Therefore, this sample provides an excellent opportunity to assess whether differences in aperture size or instrument produce significantly different, optically derived properties. In the local universe, optical emission lines are the main source of information to obtain reliable measurements of the gas-phase metallicity, ionization state of the gas, SFR, and other valuable nebular properties. However, the study of FUV spectra is crucial to fully characterize the young stellar populations and their impact on the nebular properties. Therefore, a deeper understanding of galaxy evolution requires a joint analysis of the FUV+optical CLASSY spectra. Given the different instruments and apertures used for the CLASSY FUV+optical spectra, it is important to evaluate the potential bias introduced by such observations. With our subsample of 12 CLASSY star-forming galaxies, we investigate the effect of aperture sizes on optical spectra derived nebular properties. Further, this analysis is crucial to determine whether our optically derived nebular properties are appropriate for the $2''.5$ diameter aperture of the HST/COS spectra.

The structure of this paper is as follows. We describe our sample and the optical observation in Section 2. In Section 3, we present the analysis of observations, the computation of the reddening, and aperture comparison. In Section 4, we calculate physical conditions, metallicities, and equivalent widths (EWs), and the ionization parameter of the gas for the multiple apertures. In Section 5, we compare and discuss the results and end with a summary and conclusion in Section 6.

2. Optical Spectra

The ancillary optical spectra of CLASSY comprise observations of APO/SDSS (Eisenstein et al. 2011) of 38 out of 45 objects, and multiple observations of Keck/Echelle Spectrograph and Imager (ESI) and VLT/MUSE IFU (R. L. Sanders et al. in preparation; Senchyna et al. 2019) for a small subsample of CLASSY galaxies (Berg et al. 2022). In addition, seven CLASSY galaxies were observed using long-slit spectroscopy with the Large Binocular Telescope (LBT; Hill et al. 2010) to ensure the accurate measurement of the physical properties of these galaxies (see Section 2.1). In summary, the CLASSY sample is fully covered by optical spectra for different observational sets available (Berg et al. 2022; James et al. 2022) and follow-up observations. The telescope and instruments used for the optical observations in this paper are listed in Table 1.

In this work, we have selected the 12 star-forming galaxies from the CLASSY sample having optical spectra with multiple aperture sizes ($1''.0$ – $3''.0$), observational modes (long-slit and IFU model), and spectral resolutions. In particular, the IFU data allow us to map the gas emission using different aperture sizes,

Table 1
Multiple Optical Observations of the 12 CLASSY Star-forming Galaxies Analyzed in This Work

Galaxy	Alt. Name	R.A. (hh:mm:ss)	Decl. (\pm dd:mm:ss)	z	Telescope /Instrument	Aperture Extraction	Aperture Size (kpc)	$R_{100}/2$ (")	Reference
1. J0021+0052		00:21:01.03	+00:52:48.08	0.098	APO/SDSS	3" circ	5.43	1.66	Eisenstein et al. (2011)
2. J0808+3948		08:08:44.28	+39:48:52.51	0.0912	VLT/MUSE	2"5 circ	4.52	2.90	ESO 0104.D-0503; PI: Anderson
3. J0942+3547	CG-274, SB 110	09:42:52.78	+35:47:25.98	0.0149	APO/SDSS	3" circ	0.91	3.4	Eisenstein et al. (2011)
4. J0944-0038	CGCG 007-025, SB 2	09:44:01.87	-00:38:32.18	0.005	Keck/ESI	1" \times 2"	0.30		R. L. Sanders et al. (in prep.)
5. J1024+0524	SB 36	10:24:29.25	+05:24:51.02	0.033	APO/SDSS	3" circ	1.98	2.75	Eisenstein et al. (2011)
6. J1044+0353		10:44:57.79	+03:53:13.10	0.0129	Keck/ESI	1" \times 2"	0.66		R. L. Sanders et al. (in prep.)
7. J1129+2034	SB 179	11:29:14.15	+20:34:52.01	0.005	APO/SDSS	3" circ	0.80	3.10	Eisenstein et al. (2011)
8. J1132+5722	SBSG 1129+576	11:32:35.35	+57:22:36.39	0.018	VLT/MUSE	2"5 circ	0.66		ESO 0103.B-0531; PI: Erb
9. J1148+2546	SB 182	11:48:27.34	+25:46:11.77	0.045	LBT/MODS	1" \times 2"5	0.26	4.20	Berg et al. (2021)
10. J1323-0132		13:23:47.52	-01:32:51.94	0.022	APO/SDSS	3" circ	0.31		Eisenstein et al. (2011)
11. J1418+2102		14:18:51.12	+21:02:39.84	0.009	Keck/ESI	1" \times 2"	0.10		R. L. Sanders et al. (in prep.)
12. J1545+0858	1725-54266-068	15:45:43.44	+08:58:01.34	0.038	APO/SDSS	3" circ	1.10	4.05	Eisenstein et al. (2011)
					Keck/ESI	1" \times 2"	0.37		Senchyna et al. (2019)
					APO/SDSS	3" circ	0.37	1.33	Eisenstein et al. (2011)
					Keck/ESI	1" \times 2"	0.88		R. L. Sanders et al. (in prep.)
					LBT/MODS	1" \times 2"5	0.88		This work
					APO/SDSS	3" circ	1.33	1.66	Eisenstein et al. (2011)
					LBT/MODS	1" \times 2"5	0.44		This work
					APO/SDSS	3" circ	0.55	2.84	Eisenstein et al. (2011)
					VLT/MUSE	2"5 circ	0.46		ESO 0103.B-0531; PI: Erb
					LBT/MODS	1" \times 2"5	0.18		Berg et al. (2021)
					APO/SDSS	3"0 circ	2.26	2.54	Eisenstein et al. (2011)
					LBT/MODS	1" \times 2"5	0.75		This work

Note. The columns indicate the (1) galaxy ID, (2) alternative name, (3–4) coordinates of the objects (J2000), (5) redshift, (6) telescope, instrument, or survey for each observation, (7) aperture-extraction size, (8) physical size within an aperture size of 3" for SDSS, 2"5 for MUSE and 1" for LBT/MODS, Keck/ESI, and IFU aperture of 2"5 and 3"0 apertures for VLT/MUSE and APO/SDSS, (9) the total galaxy radius represented as ($\sim R_{100}/2$) and derived using r -band images of Pan-STARRS (Berg et al. 2021) (see also Section 5.1), and (10) references for the sample.

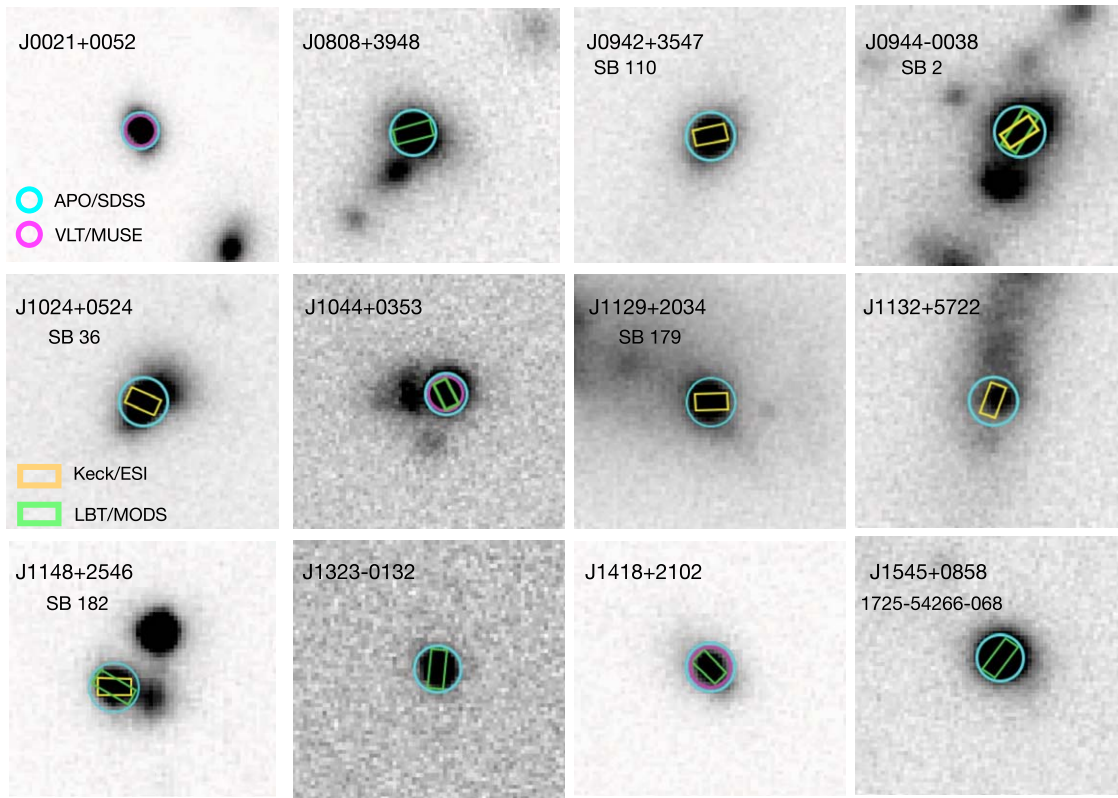


Figure 1. FoV optical images of Pan-STARRS in the r band for 12 star-forming galaxies of CLASSY. The $3''$ SDSS aperture used for the optical spectra is shown as a cyan circle and the $2''.5$ MUSE aperture as a magenta circle, whose diameter and pointing are the same as the HST/COS $2''.5$ aperture. We also highlight for comparison the $1'' \times 2''.5$ LBT/MODS slit (green box) and $1'' \times 2''$ Keck/ESI slit (orange box). The position of the apertures is centered at the brightest emission knot of each galaxy using SDSS r images. The labels show the ID of each galaxy used in this study and the alternative name for some objects. North up and east to the left.

which provides a better comparison between the different observations of this sample, e.g., to analyze the results obtained using the same aperture as in HST/COS (Berg et al. 2022; James et al. 2022).

In Figure 1, we show the optical images of Pan-STARRS²⁰ in the r band for the 12 galaxies in this study. We also overlay the aperture at the observed position angle. SDSS and MUSE observations are indicated with circular apertures of $3''$ and $2.5''$ in diameter, respectively. ESI and LBT apertures have a size of $1''$ wide with a 1D extraction box of $\sim 1'' \times 2''$ and $1'' \times 2.5''$, respectively. In Figure 1, we show the extraction sampling for each aperture. Although most of the galaxies show extended emission, the multiple apertures are covering the bright emission region of each galaxy.

To identify and compare the different aperture observations, we simply refer to the observations as SDSS, LBT, MUSE, and ESI for the rest of the paper.

2.1. LBT/MODS Observations

Here, we present new optical spectra for seven CLASSY galaxies using the Multi-Object Double Spectrographs (MODS; Pogge et al. 2010) mounted on the LBT (Hill et al. 2010). The LBT spectra of two of these galaxies (J1044+0353 and J1418+2102) have already been reported in Berg et al. (2021). The optical LBT/MODS spectra of the remaining five CLASSY galaxies were obtained on the UT dates of 2021 February 11–12 and March 17–18, respectively. MODS has a large wavelength coverage of 3200–10000 Å with a moderate

spectral resolution of $R \sim 2000$. The blue and red spectra were obtained simultaneously using the G400L (400 lines mm^{-1}) at $R \approx 1850$ and G670L (250 lines mm^{-1}) at $R \approx 2300$ gratings. The slit length was $60''$ with a width of $1''$. To minimize flux losses due to atmospheric differential refraction (Filipenko 1982), the slit was oriented along the parallactic angle at half the total integration at airmasses ranging between 1.05 and 1.31. Each object was observed with a total exposure time of 45 minutes (3×900 s exposures). Figure 1 shows the slit position and orientation of the LBT/MODS observations for J0808+3948, J0944-0038, J1148+2546 (SB 182), J1323-0132, and J1545+0858 (1725-54266-068). For comparison purposes, the LBT/MODS slit has been truncated ($1'' \times 2''.5$) to show the extraction region of the observation. The slit was centered on the highest surface brightness knots of optical emission based on SDSS r -band images, following the position of the HST/COS aperture of each CLASSY galaxy in the UV (Berg et al. 2022).

We use the CHAOS project’s data reduction pipeline (Berg et al. 2015; Croxall et al. 2016; Rogers et al. 2021) to reduce the LBT/MODS observations. To correct for bias and the flat field we apply the modsCCDRed²¹ Python programs to the standard stars, science objects, and calibration lamps. The resulting CCD images are used in the beta version of the MODS reduction pipeline²², which runs within the XIDL²³ reduction package. We perform sky subtraction, wavelength

²⁰ <https://panstarrs.stsci.edu/>

²¹ <https://github.com/rwpogge/modsCCDRed>

²² <http://www.astronomy.ohio-state.edu/MODS/Software/modsIDL/>

²³ <https://www.ucolick.org/~xavier/IDL/>

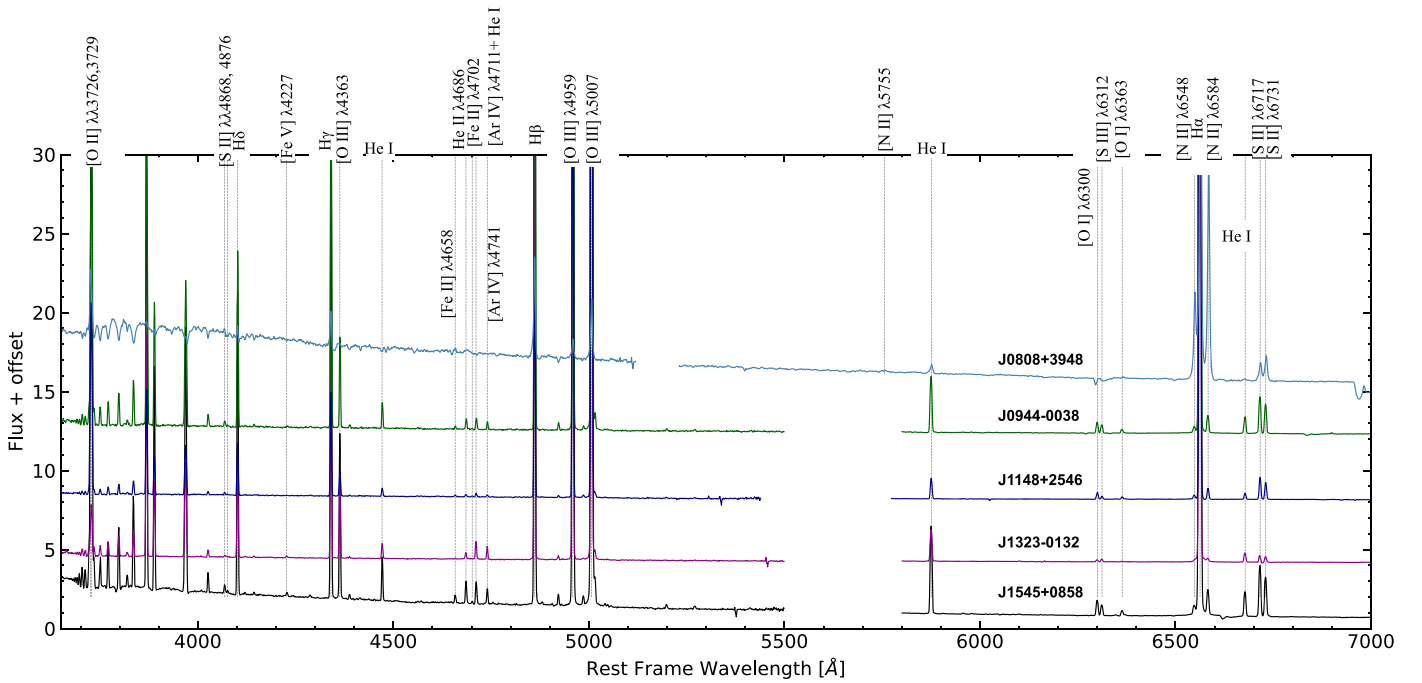


Figure 2. New optical LBT/MODS spectra of five CLASSY galaxies. The dotted lines indicate the main emission lines used in this study. F_{λ} is units of 10^{-16} ergs $^{-1}$ s $^{-1}$ cm $^{-2}$ Å $^{-1}$. We added an offset vertically for display with the exception of J1545+0858. The offset corresponds to 4, 8, 12, and 14 for J1323-0132, J1148+2546, J0944-0038, and J0808+3948, respectively. The emission lines for these spectra used in this study are reported in Table 3, and the complete version of all emission lines of MODS/LBT spectra are reported in M. Mingozi et al. (in preparation).

calibration, and flux calibration using the standard stars Feige 34, Feige 67, and G191-B2B. In Figure 2, we show the one-dimensional spectra for these galaxies. We have labeled the main emission line features. Note that with the exception of J0808+3948, the rest of the galaxies shows the very high-ionization emission line He II $\lambda 4686$ (Berg et al. 2021).

2.2. Archival Optical Spectra

Berg et al. (2022) provide a detailed description of the optical observations for CLASSY, while the scaling of the optical data to UV data is presented in M. Mingozi et al. (in preparation). Here, we give a brief summary of the main characteristics of the CLASSY galaxies relevant to this study. In Table 1, we list the optical observations of the selected galaxies. It includes the identification of the galaxy that we use in this work, the alternative names used in the literature, the coordinates, the observational ancillary, aperture size extraction of the observations, and the optical size of each galaxy represented as the total galaxy radius, ($\sim R_{100}/2$) (see Section 5.1).

APO/SDSS: The SDSS sample comprises 12 observations of 3" fiber diameter with a wavelength range of 3800–9200 Å and spectral resolution of $R \approx 1500$ –2500 (Eisenstein et al. 2011). This wavelength range allows for the measurement of the main emission lines necessary for the analysis of the physical properties of these galaxies. We use this sample as a reference to compare with the rest of the observations since the aperture size and center are similar to those of HST/COS data (Berg et al. 2022).

VLT/MUSE: We gathered archival VLT/MUSE IFU data for three CLASSY galaxies, J0021+0052 (PI: Anderson), J1044, and J1418 (PI: Dawn Erb) (see Table 1). These observations cover a wavelength range of 4300–9300 Å at a spectral resolution of $R \approx 2000$ –3500, and a field of view (FoV) of

$1' \times 1'$. For the analysis of this sample, we have extracted one-dimensional spectrum using the same 2".5 HST/COS aperture. As an additional analysis, we extracted one-dimensional spectra using different aperture sizes ranging from 1"–7".5 in diameter in steps of 0".5. With such spectra, we study the variations in the physical properties with respect to the aperture size. This analysis is discussed in Section 5.5.

We refer to this sample as VLT/MUSE or IFU to distinguish it from long-slit spectra. Note that we have extracted the integrated flux using an aperture size of 2".5 resulting in one-dimensional spectra.

Keck/ESI: This sample comprises six CLASSY galaxies with high spectral resolution using the ESI on board Keck II. These spectra cover a rest-frame wavelength ranging from approximately 3800–10000 Å, at a spectral resolution of $R \approx 4700$ at 1" slit width. The long-slit spectra of these galaxies were obtained from Senchyna et al. (2019) and R. L. Sanders et al. (in preparation).

3. Emission Line Measurements

3.1. Emission Line Fluxes

To prepare the spectra for emission line measurements, the optical spectra were corrected by Galactic extinction using the Green et al. (2015) extinction maps included in the PYTHON DUSTMAPS package (Green 2018), and the Cardelli et al. (1989) reddening law. Next, since the Balmer lines are affected by stellar absorption, we model the stellar continuum using the Starlight²⁴ spectral synthesis code (Cid Fernandes et al. 2005) and subtract it. To do so, we follow the successful continuum-subtraction method of the CHAOS survey (Berg et al. 2015) and assume the stellar population models of

²⁴ www.starlight.ufsc.br

Bruzual & Charlot (2003) with the initial mass function (IMF) of Chabrier (2003). We use a set of simple stellar populations that span 25 ages (1 Myr–18 Gyr) and six metallicities ($0.05 Z_{\odot} < Z < 2.5 Z_{\odot}$).

Using the continuum-subtracted spectra, we fit the emission lines with Gaussian profiles using the Python package LMFIT.²⁵ Specifically, we simultaneously fit sections of nearby lines ($<200 \text{ \AA}$), while constraining the offset from line centers and the line width. This method also allows us to simultaneously fit weak and blended lines with a higher degree of accuracy. Since the [O II] $\lambda\lambda 3726, 3729$ lines are blended in LBT and SDSS observations, we have fitted two Gaussian profiles to constrain the flux measurements in such lines. The errors in the flux were calculated using the expression reported in Berg et al. (2013) and Rogers et al. (2021). Note that for the LBT/MODS spectra of J1044+0353, and J1418+2102, we adopted the line fluxes reported in Berg et al. (2021). To ensure significant emission line detections, we only use lines with a signal-to-noise ratio of $S/N > 3$.

The auroral emission lines used to measure temperatures are intrinsically faint and so require careful consideration. Therefore, we inspected the [O III] $\lambda 4363$, [N II] $\lambda 5755$, [S III] $\lambda 6312$, and [O II] $\lambda\lambda 7320, 7330$ auroral lines fits to ensure a well-constrained flux measurement. As a secondary check, we measured these faint T_e sensitive lines by hand using the integration tool in IRAF²⁶ Both the PYTHON and IRAF methods produced consistent flux values. Additionally, for high-metallicity star-forming galaxies ($12 + \log(\text{O}/\text{H}) > 8.4$) the [O III] $\lambda 4363$ emission line could be contaminated by [Fe II] $\lambda 4359$ (Curti et al. 2017, $12 + \log(\text{O}/\text{H}) > 8.4$). Recently, Arellano-Córdova et al. (2020) analyzed the effect of using [O III] $\lambda 4363$ blended with [Fe II] in the computation of temperature and metallicity in a sample of the Milky Way and Magellanic Cloud H II regions. These authors concluded that the use of a contaminated [O III] $\lambda 4363$ line can lead to differences in metallicity up to 0.08 dex. However, most of the objects in the present sample are metal-poor galaxies, but, we have taken into account the possible contamination of [O III] $\lambda 4363$ by [Fe II] $\lambda 4359$ in each spectrum of the sample as a precaution.

In Figure 3, we show the resulting spectrum for SDSS, LBT, and ESI of J0944-0038 (or SB 2). We subtracted the continuum from the underlying stellar population and added a small offset for a better comparison of the different spectra.

The different observations for J0944-0038 show the main emission lines used to compute the physical conditions of the nebular gas, namely, the electron density and temperature, and metallicity. These spectra contain significant He II $\lambda 4686$, [Ar IV] $\lambda\lambda 4711, 4740$, and [Fe V] $\lambda 4227$ emissions, indicative of a very high-ionization gas in this galaxy (see the dashed lines in Figure 3). Such very high-ionization conditions of the gas were reported by Berg et al. (2021) for J1044+0353 and J1418+2102. Additionally, 11 galaxies in our sample have He II and [Ar IV] line detections, but no [Fe V] $\lambda 4227$ detections. Note that for J0944-0038 (see Figure 3), there is an odd artifact at $\approx 5100 \text{ \AA}$ in the SDSS spectrum that is not detected in the LBT or ESI spectra. This feature is likely an

artifact of the SDSS reduction process, but it does not affect our emission line flux measurements.

3.2. Reddening Corrections

Before calculating nebular properties, the emission lines must first be corrected for reddening due to dust with the galaxy. To do so, we calculate the color excess, $E(B - V)$, for three Balmer decrements ($H\alpha/H\beta$, $H\gamma/H\beta$, and $H\delta/H\beta$) using the expression

$$E(B - V) = \frac{-2.5}{\kappa(I_{\lambda}) - \kappa(I_{H\beta})} \times \log_{10} \left[\frac{(I_{\lambda}/I_{H\beta})_{\text{theo.}}}{(I_{\lambda}/I_{H\beta})_{\text{obs.}}} \right], \quad (1)$$

where $\kappa(\lambda)$ is the value of the attenuation curve at the corresponding wavelength, and $(I_{\lambda}/I_{H\beta})_{\text{theo.}}$ and $(I_{\lambda}/I_{H\beta})_{\text{obs.}}$ are theoretical and observed Balmer ratios, respectively. We adopt the reddening law of Cardelli et al. (1989) to calculate $\kappa(\lambda)$.

To calculate the color excesses, we use three Balmer ratios, $H\alpha/H\beta$, $H\gamma/H\beta$, and $H\delta/H\beta$, for each galaxy, with a few exceptions (see Section 2):

1. For the MUSE spectra of J1044+0353 and J1418+2102, the limited spectral coverage limits the $E(B - V)$ calculations to only the $H\alpha/H\beta$ ratio.
2. For the SDSS spectra of J0944-0038, the $H\alpha$ emission line shows an asymmetric odd extension previously reported by Senchyna et al. (2017), which is not visible in MUSE and ESI spectra.
3. For the ESI spectra of J1129+2034, the $H\alpha$ emission line is saturated and so cannot be used.
4. For the ESI spectra of J1148+2546, the $H\gamma$ emission line is affected by a detector artifact and so cannot be used.
5. For the ESI spectra of J1024+0524, both the $H\gamma$ and [O III] $\lambda 4363$ emission lines are affected by a detector artifact and so cannot be used.
6. For the LBT spectra of J1148+2546, the $H\delta$ is affected by an artifact and so cannot be used.

We calculate $E(B - V)$ values following the approach of Berg et al. (2022), which iteratively calculates the electron temperature and density, and $E(B - V)$ values. We calculate the initial electron temperature using $T_e[\text{O III}]$ ([O III] ($\lambda\lambda 4959, 5007$)/ $\lambda 4363$ when measured, and other available temperature diagnostics when not (e.g., $T_e[\text{S III}]$ for MUSE). Using this temperature and assuming the [S II] densities reported in Berg et al. (2022) and Case B recombination, we calculated the theoretical ratios of $H\alpha$, $H\beta$, $H\gamma$, and $H\delta$ relative to $H\beta$. The iterative process stops when the difference in $T_e \leq 20 \text{ K}$. Note that in each iteration, the line intensities used to calculate temperature and density were corrected for reddening. For comparison, we have also calculated the $E(B - V)$ values for the SDSS sample assuming a unique value of $T_e = 10000 \text{ K}$ and $n_e = 100 \text{ cm}^{-3}$ to derive the theoretical $H\alpha/H\beta$, $H\gamma/H\beta$, and $H\delta/H\beta$ ratios (a typical approach for star-forming regions). We find that the difference between this approach and our iterative procedure is up to ~ 0.04 dex, in particular, when $T_e > 10,000 \text{ K}$. The uncertainties of the $E(B - V)$ values were estimated using a Monte Carlo simulation, generating 500 random values and assuming a Gaussian distribution with a sigma equal to the uncertainty of the associated Balmer ratio. The final adopted value of $E(B - V)$ for each spectrum is the weighted mean after discarding any negative $E(B - V)$.

²⁵ Nonlinear Least-squares Minimization and Curve Fitting: <https://github.com/lmfit/lmfit-py>.

²⁶ IRAF is distributed by the National Optical Astronomy Observatory, which is operated by the Association of Universities for Research in Astronomy, Inc., under a cooperative agreement with the National Science Foundation.

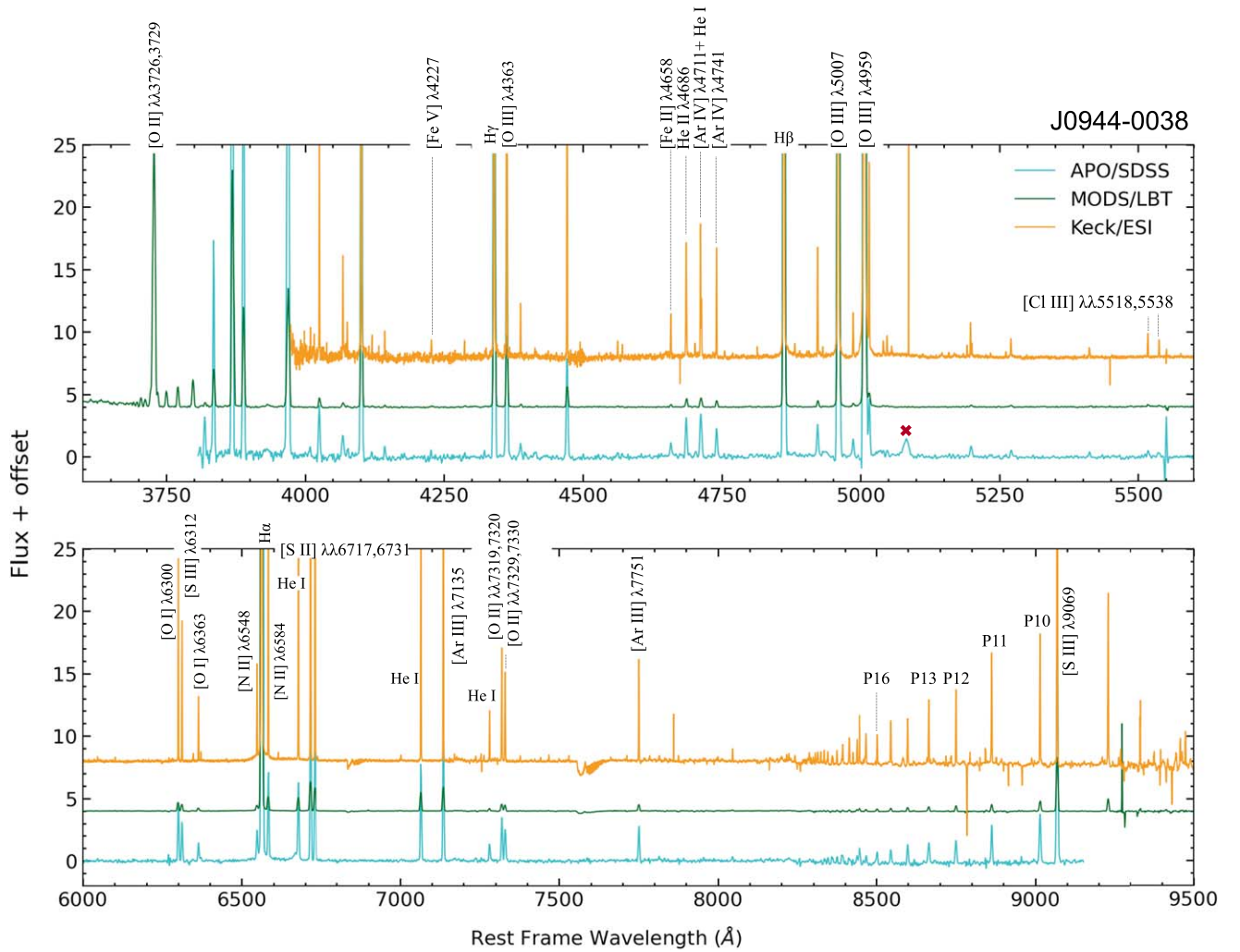


Figure 3. Comparison of the optical spectra of J0944 (or SB 2). These spectra were observed using different instruments with different aperture sizes (APO/SDSS: 3" diameter, LBT/MODS: 1" slit, and Keck/ESI: 1" slit). For a better visual comparison, the flux scale is arbitrarily offset between the spectra. The labels indicate the emission lines used to calculate the physical properties of star-forming galaxies. In the SDSS spectrum, we identify an unknown emission artifact (red x), but note that it does not affect the flux measurements of the emission lines around.

In Table 2, we list the galaxy ID, the observational data, the $E(B - V)$ values for each Balmer line ratio (Columns 3–5), and the adopted $E(B - V)$ value (Column 6). In Section 5, we discuss the differences in $E(B - V)$ implied by the different Balmer lines with respect to $H\beta$ and other physical properties of CLASSY galaxies.

Finally, emission lines relative to $H\beta$ ($I_\lambda/I_{H\beta}$) were corrected for reddening using the final $E(B - V)$ values reported in Table 2 and the reddening function $f(\lambda)$ normalized to $H\beta$ by Cardelli et al. (1989). Note that at optical wavelengths, the variation in extinction with λ is small (Shivaei et al. 2020; Reddy et al. 2016). Therefore, our results are not affected by our choice of the extinction law selected for this sample. The final errors are the result of adding in quadrature the uncertainties in the measurement of the fluxes and the error associated with the fits. We report the resulting emission line intensities for the optical spectra analyzed in this work in Table 3. Note that the optical emission lines are reported for the entire CLASSY sample in M. Mingozi et al. (in preparation), but only for a single spectrum per galaxy. Given the comparison of multiple spectra per galaxy in this work, we

remeasured the emission lines of spectra in M. Mingozi et al. (in preparation) for consistency.

4. Physical Conditions and Chemical Abundances

We use the PyNeb package (version 1.1.14) (Luridiana et al. 2015) in Python to calculate the physical conditions and chemical abundances. We use atomic data for a five-level atom model (De Robertis et al. 1987). We use the transition probabilities of Froese Fischer & Tachiev (2004) for O^+ , O^{2+} , N^+ , and S^+ , and of Podobedova et al. (2009) for S^{2+} . For the collision strengths, we use Kisielius et al. (2009) for O^+ , Aggarwal & Keenan (1999) for O^{2+} , Tayal (2011) for N^+ , Tayal (2011) for S^+ , and Hudson et al. (2012) for S^{2+} .

4.1. Nebular Density and Temperature

To compute the electron density (n_e), we use $[S II] \lambda 6717/\lambda 6731$ for all the set of observations and $[O II] \lambda 3726/\lambda 3727$ for LBT spectra and four SDSS spectra. We calculate the electron temperature using the line intensity ratios:

Table 2
Physical Properties of the 12 CLASSY Star-forming Galaxies from the Different Apertures Analyzed in This Work

Galaxy	Telescope /Instrument	H α /H β	$E(B - V)$ H γ /H β	H δ /H β	$E(B - V)$ Adopted	EW(H α) (\AA)	EW([O III] λ 5007) (\AA)
J0021+0052	APO/SDSS	0.142 \pm 0.010	0.116 \pm 0.021	0.120 \pm 0.025	0.135 \pm 0.009	496 \pm 15	400 \pm 9
	VLT/MUSE	0.237 \pm 0.012	0.150 \pm 0.021	...	0.214 \pm 0.011	520 \pm 10	430 \pm 9
J0808+3948	APO/SDSS	0.331 \pm 0.039	0.007 \pm 0.124	0.214 \pm 0.144	0.296 \pm 0.036	69 \pm 2	7 \pm 1
	LBT/MODS	0.215 \pm 0.026	0.226 \pm 0.04	0.062 \pm 0.062	0.202 \pm 0.020	77 \pm 2	7 \pm 1
J0942+3547	APO/SDSS	0.021 \pm 0.006	-0.015 \pm 0.014	-0.030 \pm 0.017	0.021 \pm 0.006	490 \pm 24	461 \pm 9
	Keck/ESI	0.169 \pm 0.003	0.063 \pm 0.008	0.007 \pm 0.007	0.134 \pm 0.003	453 \pm 19	424 \pm 10
J0944-0038	APO/SDSS	...	0.201 \pm 0.014	0.185 \pm 0.014	0.193 \pm 0.009	...	1464 \pm 68
	Keck/ESI	0.169 \pm 0.003	0.063 \pm 0.008	0.007 \pm 0.007	0.134 \pm 0.003	1788 \pm 46	1798 \pm 16
	LBT/MODS	0.164 \pm 0.012	0.172 \pm 0.022	0.180 \pm 0.017	0.170 \pm 0.009	1576 \pm 31	2121 \pm 21
J1024+0524	APO/SDSS	0.001 \pm 0.007	0.097 \pm 0.014	0.064 \pm 0.017	0.025 \pm 0.006	523 \pm 21	513 \pm 15
	Keck/ESI	0.071 \pm 0.009	...	0.016 \pm 0.016	0.055 \pm 0.008	503 \pm 12	515 \pm 14
J1044+0353	APO/SDSS	0.118 \pm 0.011	0.057 \pm 0.017	0.003 \pm 0.015	0.072 \pm 0.008	1620 \pm 84	1212 \pm 41
	VLT/MUSE	0.088 \pm 0.007	0.088 \pm 0.007	1664 \pm 20	1509 \pm 24
	LBT/MODS	0.086 \pm 0.009	0.231 \pm 0.018	0.231 \pm 0.015	0.14 \pm 0.007	1594 \pm 56	1568 \pm 40
J1129+2034	APO/SDSS	0.220 \pm 0.010	0.126 \pm 0.015	...	0.191 \pm 0.009	1220 \pm 60	935 \pm 42
	Keck/ESI	...	0.081 \pm 0.018	0.175 \pm 0.020	0.125 \pm 0.013	...	1440 \pm 14
J1132+5722	APO/SDSS	0.035 \pm 0.009	0.07 \pm 0.024	0.004 \pm 0.040	0.038 \pm 0.008	400 \pm 23	175 \pm 5
	Keck/ESI	0.051 \pm 0.010	0.199 \pm 0.064	0.015 \pm 0.071	0.054 \pm 0.010	587 \pm 56	283 \pm 28
J1148+2546	APO/SDSS	0.113 \pm 0.007	0.147 \pm 0.013	0.114 \pm 0.016	0.119 \pm 0.006	879 \pm 26	956 \pm 11
	Keck/ESI	0.071 \pm 0.004	...	-0.054 \pm 0.008	0.071 \pm 0.004	796 \pm 16	973 \pm 25
	LBT/MODS	0.060 \pm 0.012	0.180 \pm 0.019	...	0.093 \pm 0.010	1051 \pm 30	1510 \pm 67
J1323-0132	APO/SDSS	0.118 \pm 0.009	0.202 \pm 0.017	0.239 \pm 0.022	0.147 \pm 0.007	1561 \pm 33	2080 \pm 83
	LBT/MODS	0.109 \pm 0.010	0.192 \pm 0.020	0.204 \pm 0.015	0.146 \pm 0.008	1429 \pm 30	2281 \pm 93
J1418+2102	APO/SDSS	0.112 \pm 0.005	0.154 \pm 0.017	...	0.116 \pm 0.005	1237 \pm 85	1053 \pm 24
	VLT/MUSE	0.091 \pm 0.006	0.091 \pm 0.006	1329 \pm 22	1367 \pm 10
	LBT/MODS	0.045 \pm 0.011	0.192 \pm 0.023	0.215 \pm 0.018	0.105 \pm 0.009	1121 \pm 48	1342 \pm 48
J1545+0858	APO/SDSS	0.154 \pm 0.005	0.210 \pm 0.015	0.133 \pm 0.015	0.156 \pm 0.004	1140 \pm 33	1151 \pm 38
	LBT/MODS	0.024 \pm 0.009	0.160 \pm 0.016	0.181 \pm 0.013	0.088 \pm 0.007	1132 \pm 17	1394 \pm 32

Note. The columns indicate the (1) galaxy ID, (2) instrument/telescope of the observations, (3)–(5) $E(B - V)$ values derived using Balmer line ratios H α /H β , H γ /H β , and H δ /H β , respectively, (6) the adopted extinction value, $E(B - V)$, calculated using the weighted mean, (7) the SFR derived using H α luminosity, and (8)–(9) the EW for H α and [O III] λ 5007, respectively.

Table 3
Dereddened Emission Line Intensities Measured for the LBT/MODS Spectra for Five CLASSY Galaxies

Wavelength (\AA)	Ion	J0808+3948	J0944-0038 SB 2	J1148+2546 SB 182	J1323-0132	J1545+0858
3726.04	[O II]	42.6 \pm 3.2	36.0 \pm 2.7	46.6 \pm 3.2	9.4 \pm 1.0	26.2 \pm 1.6
3728.80	[O II]	30.6 \pm 3.0	39.2 \pm 2.3	68.7 \pm 3.3	9.4 \pm 1.0	33.4 \pm 1.6
4101.71	H δ	28.42 \pm 1.43	25.22 \pm 0.41	...	25.17 \pm 0.32	24.5 \pm 0.28
4340.44	H γ	45.69 \pm 1.06	46.61 \pm 0.69	45.2 \pm 0.5	46.26 \pm 0.49	45.62 \pm 0.42
4363.21	[O III]	...	12.42 \pm 0.43	10.2 \pm 0.3	20.15 \pm 0.38	12.87 \pm 0.27
4861.35	H β	100.0 \pm 3.0	100.0 \pm 2.0	100.0 \pm 1.1	100.0 \pm 1.0	100.0 \pm 1.0
4958.61	[O III]	18.5 \pm 1.3	198.0 \pm 5.1	208.7 \pm 4.4	245.4 \pm 4.1	193.1 \pm 3.3
5006.84	[O III]	54.5 \pm 1.7	589.2 \pm 7.8	624.8 \pm 6.5	728.6 \pm 6.2	571.4 \pm 4.8
5754.64	[N II]	1.31 \pm 0.26
6312.06	[O II]	...	1.47 \pm 0.06	1.3 \pm 0.1	0.82 \pm 0.22	1.09 \pm 0.04
6548.05	[N II]	65.52 \pm 2.43	1.07 \pm 0.8	1.8 \pm 0.8	0.42 \pm 0.6	0.97 \pm 0.51
6562.79	H α	299.5 \pm 9.8	269.0 \pm 4.7	271.7 \pm 4.1	266.9 \pm 3.2	260.9 \pm 2.9
6583.45	[N II]	196.56 \pm 7.29	3.22 \pm 2.41	5.5 \pm 2.3	1.25 \pm 1.81	2.91 \pm 1.52
6716.44	[S II]	20.54 \pm 0.76	6.84 \pm 0.16	11.3 \pm 0.3	1.75 \pm 0.33	5.65 \pm 0.26
6730.82	[S II]	26.72 \pm 0.92	5.37 \pm 0.14	8.7 \pm 0.2	1.55 \pm 0.33	4.41 \pm 0.26
7319.92	[O II]	...	1.39 \pm 0.05	...	0.44 \pm 0.04	...
7339.79	[O II]	...	1.14 \pm 0.05	...	0.37 \pm 0.04	...
9068.60	[S III]	29.65 \pm 1.55	10.1 \pm 0.33	10.8 \pm 0.5	4.41 \pm 0.21	7.87 \pm 0.21
9530.60	[S III]	73.23 \pm 3.84	24.66 \pm 0.69	26.1 \pm 0.9	10.9 \pm 0.52	19.45 \pm 0.51
$E(B - V)$		0.202 \pm 0.020	0.170 \pm 0.009	0.093 \pm 0.010	0.146 \pm 0.008	0.08 \pm 0.007
$F_{H\beta}$		38.2 \pm 0.8	190.1 \pm 1.7	70.1 \pm 0.60	109.3 \pm 0.7	349.1 \pm 2.3

Note. Intensity ratios are reported with respect to $I(H\beta) = 100$, where the observed H β fluxes (in units of 10^{-16} erg s $^{-1}$ cm $^{-2}$) are reported in the second to last row. The color-excess values, $E(B - V)$, used to redden the line ratios are listed in the last row.

[O II] ($\lambda\lambda 3726, 3729$)/($\lambda\lambda 7319, 7320 + \lambda\lambda 7330, 7331$),²⁷ [N II] ($\lambda\lambda 6548, 6584$)/ $\lambda 5755$, [S III] ($\lambda\lambda 9069, 9532$)/ $\lambda 6312$, and [O III] ($\lambda\lambda 4959, 5007$)/ $\lambda 4363$, when they are available. The [S III] $\lambda\lambda 9069, 9532$ and [O II] $\lambda\lambda 7320, 7330$ ratios can be affected by telluric and absorption features (Stevenson 1994). We carefully check the different spectra for the presence of emission/absorption features that can affect those lines. For LBT spectra, we measured the flux of both [S III] $\lambda 9069$ and [S III] $\lambda 9532$ and compared the observed ratio to the theoretical ratio of [S III] $\lambda 9532/\lambda 9069 = 2.47$ from `PyNeb` to test for contamination by absorption bands. If the observed ratio of [S III] $\lambda 9532/\lambda 9069$ is within the uncertainty of the theoretical ratio, we use both lines to compute T_e ([S III]). For [S III] ratios that are outside this range, we discarded [S III] $\lambda 9069$ when the observed ratio is larger than the theoretical ratio, and discarded [S III] $\lambda 9532$ when the theoretical one is lower following Arellano-Córdova et al. (2020) and Rogers et al. (2021). Since it was only possible to measure [S III] $\lambda 9069$ for most of the other spectra, we used it with the [S III] theoretical ratio to estimate [S III] $\lambda 9532$.

We also inspected [O II] $\lambda\lambda 7320, 7330$ for possible contamination by telluric absorption bands (Stevenson 1994). For the observations considered here, absorption bands were not detected around the red [O II] lines. Note that due to the redshift of these galaxies, some other lines can also be affected by absorption bands. The [S II] $\lambda 6731$ line of J1323-0132 of LBT is contaminated by a telluric absorption band, which might impact the results of the n_e measurement (see Section 5 for further discussion). Additionally, the strongest emission lines in the optical spectra are at risk of saturating. We, therefore, carried out a visual inspection of the [O III] $\lambda 5007$ line and also compared its flux to the theoretical ratio of [O III] $\lambda 5007/\lambda 4959$ for our sample. If [O III] $\lambda 5007$ is saturated, we instead used [O III] $\lambda 4959$ to estimate [O III] $\lambda 5007$ using the theoretical ratio of 2.98 from `PyNeb`.

In Table 4, we present the results of n_e in Columns 2 and 3 and T_e in Columns 3–7 for the whole sample. The uncertainties were calculated using Monte Carlo simulations in a way similar to $E(B - V)$.

In the H II regions, a temperature gradient is expected in the interior of the nebula, associated with its different ionization zones (low, intermediate, and high ionization) based on the ionization potential energy (electronvolts) of the ions present in the gas (Osterbrock 1989; Osterbrock & Ferland 2006). To characterize the temperature structure of the nebular gas, we use T_e ([O III]) as representative of the high-ionization region and T_e ([O II]) or T_e ([N II]) as representative of the low-ionization region. If both T_e ([O II]) and T_e ([N II]) are measured, we prioritize T_e ([O II]) to characterize the low-ionization region. This is because at low metallicity the [N II] $\lambda 5755$ line is too faint and the uncertainties associated with T_e are large in comparison to T_e ([O II]) (see Table 4). When T_e ([O II]), T_e ([N II]), or T_e ([O III]) are not detected, we use the temperature relation of Garnett (1992) to estimate those temperatures, which are based on the photoionization models:

$$T_e[\text{O II}] \approx T_e[\text{N II}] = 0.7T_e[\text{O III}] + 3000 \text{ K} \quad (2)$$

and

$$T_e[\text{S III}] = 0.83T_e[\text{O III}] + 1700 \text{ K}. \quad (3)$$

For those cases where the only available temperature is T_e ([S III]), J1014 and J1418 of MUSE, we use the empirical relation from Rogers et al. (2021) to estimate T_e ([O II]):

$$T_e[\text{O II}] \approx T_e[\text{N II}] = 0.68T_e[\text{S III}] + 2800 \text{ K}. \quad (4)$$

Figure 4 shows different temperature relations implied by the multiple apertures of CLASSY galaxies. In the left panel of this figure, we show the T_e ([O III])– T_e ([S III]) relation. The temperature relationships based on photoionization models of Garnett (1992) and Izotov et al. (2006) (for low metallicity regime) are indicated by solid and dashed lines, respectively. In principle, the sample of galaxies follows both temperature relations, in particular, the LBT and ESI samples. However, at low temperatures ($T_e < 14,000$ K), the relationship of Garnett (1992) is consistent with our results for the ESI and SDSS observations (although few galaxies are present in these low-temperature regimes). As such, we feel confident in using the temperature relation of Garnett (1992) to estimate T_e ([O III]) from T_e ([S III]) when a unique T_e is available.

Low-ionization temperatures, T_e ([N II]) and T_e ([O II]) are available for few CLASSY galaxies in this sample. However, in the middle and right panels of Figure 4, we present the low-ionization temperatures versus T_e ([O III]) and T_e ([S III]), respectively. The solid and empty symbols represent the results for T_e ([N II]) and T_e ([O II]). For J0021+0051, it was possible to calculate both T_e ([N II]) and T_e ([O II]) using the SDSS spectrum (see also Table 4). We find that T_e ([N II]) and T_e ([O II]) show a difference of 900 K. However, the uncertainty derived to T_e ([N II]) is large with respect to T_e ([O II]). Such uncertainty might mainly be associated with the measurement of the faint [N II] $\lambda 5755$ auroral in the SDSS spectrum. On the other hand, T_e ([N II]) and T_e ([O II]) are expected to be similar due to that those temperatures are representative of the low-ionization zone of the nebula (see Equations (2) and (4)). Previous works have studied the behavior of the T_e ([N II]) and T_e ([O II]) relation using observations of H II regions and star-forming galaxies (see, e.g., Izotov et al. 2006; Pérez-Montero et al. 2007; Croxall et al. 2016; Rogers et al. 2021; Zurita et al. 2021). Such results show a discrepancy and large dispersion between T_e ([N II]) and T_e ([O II]), whose origin might be associated with the measurements of the [N II] $\lambda 5755$ auroral in the case of T_e ([N II]). For T_e ([O II]), the [O II] $\lambda\lambda 7320, 7330$ auroral lines have a small contribution of recombination, depending on the electron density and reddening, and those lines can be contaminated by telluric lines (e.g., Stasińska 2005; Pérez-Montero et al. 2007; Rogers et al. 2021; Arellano-Córdova et al. 2020). Therefore, the impact of using T_e ([O II]) in the determination of O^+ and the total oxygen abundance might be more uncertain in low-ionization objects, i.e., high-metallicity environments ($12 + \log(O/H) \gtrsim 8.2$). In Figure 4, we find that those results for T_e ([O II]) (empty symbols) follow the relationships in Garnett (1992) and Izotov et al. (2006). As such, we also use the relationship in Garnett (1992) to estimate the low-ionization temperature, T_e ([O II]), when this temperature is not available.

On the other hand, the right panel of Figure 4 also shows the T_e ([N II])– T_e ([S III]) relation for the ESI and LBT (T_e ([O II])) observations. Such a relationship was previously presented for local star-forming regions by Croxall et al. (2016), Berg et al. (2020), and Rogers et al. (2021) showing a tight relation

²⁷ Due to low spectral resolution it is not possible to resolve these lines, hereafter, referred to as [O II] $\lambda 3727$ and [O II] $\lambda\lambda 7320, 7330$.

Table 4
Physical Conditions and the Ionic and Total Oxygen Abundances for the SDSS, LBT, MUSE, and ESI Observations

Galaxy	n_e ([S II]) (cm^{-3})	n_e ([O II]) (cm^{-3})	T_e ([O II]) (K)	T_e ([N II]) (K)	T_e ([S III]) (K)	T_e ([O III]) (K)	T_e (Low) (K)	T_e (High) (K)	O^+/H^+ ($\times 10^5$)	O^{2+}/H^+ ($\times 10^5$)	12+ $\log(\text{O}/\text{H})$
APO/SDSS											
J0021+0052	90 ± 40	300 ± 80	11,600 ± 450	12,500 ± 2600	...	10,800 ± 500	11,600 ± 450	10,800 ± 500	3.7 ± 0.7	12.9 ± 2.4	8.22 ± 0.06
J0808+3948	1100 ± 250
J0942+3547	50 ± 30	17,600 ± 6200	...	12,600 ± 200	12,000 ± 200	12,600 ± 200	2.4 ± 0.2	8.3 ± 0.8	8.05 ± 0.03
J0944-0038	120 ± 30	14,100 ± 300	15,700 ± 200	14,000 ± 100	15,700 ± 200	1.00 ± 0.01	5.4 ± 0.2	7.81 ± 0.02
J1024+0524	80 ± 30	180 ± 50	13,200 ± 550	14,300 ± 200	13,200 ± 550	14,300 ± 200	1.5 ± 0.1	6.5 ± 0.4	7.90 ± 0.02
J1044+0353	240 ± 100	15,400 ± 1100	19,200 ± 300	16,500 ± 200	19,200 ± 300	0.20 ± 0.01	2.6 ± 0.1	7.44 ± 0.02
J1129+2034	90 ± 30	10,400 ± 200	10,300 ± 200	10,200 ± 100	10,300 ± 200	7.1 ± 0.7	15.1 ± 1.4	8.35 ± 0.04
J1132+1411	140 ± 60	15,000 ± 2000	17,300 ± 350	15,100 ± 900	17,300 ± 350	1.1 ± 0.3	1.6 ± 0.4	7.42 ± 0.10
J1148+2546	100 ± 30	140 ± 100	12,100 ± 350	13,900 ± 100	12,100 ± 350	13,900 ± 100	1.8 ± 0.1	8.1 ± 0.6	8.00 ± 0.02
J1323-0132	690 ± 380	17,000 ± 250	14,900 ± 100	17,000 ± 250	0.20 ± 0.01	6.0 ± 1.1	7.80 ± 0.17
J1418+2102	60 ± 40	16,200 ± 400	17,900 ± 300	15,600 ± 200	17,900 ± 300	0.40 ± 0.01	3.2 ± 0.3	7.56 ± 0.02
J1545+0858	90 ± 20	270 ± 100	11,800 ± 500	16,200 ± 200	11,800 ± 500	16,200 ± 200	0.60 ± 0.01	4.9 ± 0.3	7.74 ± 0.02
LBT/MODS											
J0808+3948	1000 ± 250	1470 ± 600	...	7700 ± 1150	7700 ± 1150	6500 ± 700	46.8 ± 22.6	11.5 ± 5.6	8.77 ± 0.24
J0944-0038	140 ± 10	480 ± 170	15,100 ± 900	...	14,900 ± 400	15,500 ± 300	15,100 ± 100	15,500 ± 300	0.62 ± 0.08	6.0 ± 0.3	7.82 ± 0.03
J1044+0353	200 ± 40	<100	18,200 ± 1400	...	17,700 ± 500	19,200 ± 200	18,200 ± 1400	19,200 ± 200	0.13 ± 0.01	2.6 ± 0.2	7.44 ± 0.02
J1148+2546	110 ± 50	100 ± 10	13,700 ± 700	13,800 ± 200	12,700 ± 100	13,800 ± 200	1.00 ± 0.10	8.3 ± 0.6	7.97 ± 0.02
J1323-0132	640 ± 650	680 ± 390	15,200 ± 2600	...	17,600 ± 3800	17,700 ± 200	15,200 ± 2600	17,700 ± 200	0.10 ± 0.01	5.2 ± 1.2	7.74 ± 0.02
J1418+2102	80 ± 40	130 ± 30	15,200 ± 850	...	14,900 ± 400	17,800 ± 200	15,200 ± 850	17,800 ± 200	0.30 ± 0.01	3.6 ± 0.3	7.60 ± 0.02
J1545+0858	130 ± 30	190 ± 100	16,000 ± 200	14,200 ± 100	16,000 ± 200	0.60 ± 0.01	5.4 ± 0.2	7.78 ± 0.02
VLT/MUSE											
J0021+0052	120 ± 40	14100 ± 1600	...	10,600 ± 400	14,100 ± 1600	10,600 ± 400	1.2 ± 0.6	13.2 ± 6.4	8.16 ± 0.09
J1044+0353	170 ± 40	21,500 ± 900	...	17,400 ± 600	23,800 ± 1000	0.10 ± 0.01	1.7 ± 0.2	7.28 ± 0.04
J1418+2102	50 ± 30	16,700 ± 400	...	14,200 ± 300	18,100 ± 500	0.60 ± 0.10	3.3 ± 0.3	7.59 ± 0.03
Keck/ESI											
J0942+3547	<100	10,200 ± 1300	11,880 ± 200	12,400 ± 200	11,700 ± 100	12,400 ± 200	3.5 ± 0.3	9.1 ± 0.8	8.10 ± 0.30
J0944-0038	100 ± 10	11,000 ± 1900	15,000 ± 200	16,700 ± 200	14,700 ± 100	16,700 ± 200	0.80 ± 0.01	4.5 ± 0.1	7.73 ± 0.01
J1024+0524	100	12,500 ± 2600	18,600 ± 1500	...	15,500 ± 400	20,400 ± 700	0.5 ± 0.1	3.1 ± 0.1	7.55 ± 0.04
J1129+2034	90 ± 20	10,200 ± 500	10,300 ± 100	9700 ± 100	10,200 ± 500	10,300 ± 200	8.9 ± 1.0	15.5 ± 1.4	8.39 ± 0.05
J1132+5722	60 ± 40	15,800 ± 1800	15,800 ± 1500	14,200 ± 1200	15,800 ± 1500	1.1 ± 0.4	2.0 ± 0.7	7.50 ± 0.13
J1148+2546	130 ± 20	10,800 ± 1400	14,100 ± 200	14,200 ± 200	12,900 ± 100	14,200 ± 200	1.5 ± 0.1	7.9 ± 0.2	7.97 ± 0.01

Note. For the ionic and total abundances we used $T_e(\text{low})$ and $T_e(\text{high})$, see Section 4. The ionic abundances, X^{i+}/H^+ and the total oxygen abundance in units of 12+ $\log(\text{O}/\text{H})$.

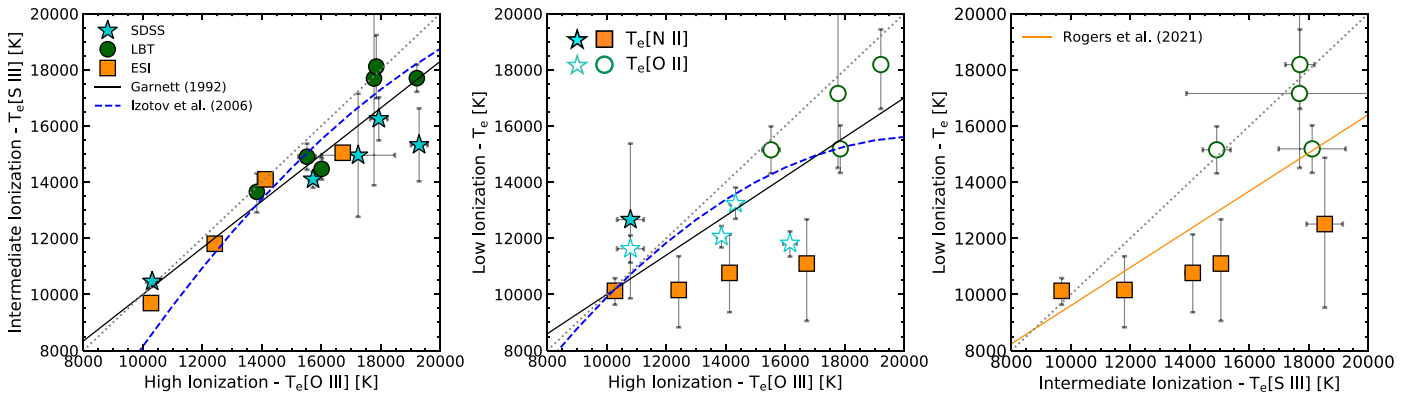


Figure 4. *Left:* the $T_e([\text{O III}])$ – $T_e([\text{S III}])$ relation for some galaxies with SDSS, LBT, and ESI spectra. The multiple apertures are labeled at the top of the left panel. The solid and dashed lines represent the temperature relations from Garnett (1992) and Izotov et al. (2006) (low metallicity regime). *Middle:* the $T_e([\text{O III}])$ – $T_e([\text{N II}])$ relation for the ESI and SDSS sample indicated with solid symbols and the $T_e([\text{O III}])$ – $T_e([\text{O II}])$ relation for the LBT and SDSS sample represented with empty symbols. *Right:* the $T_e([\text{S III}])$ – $T_e([\text{N II}])$ relation for the ESI results represented by solid symbols and the $T_e([\text{S III}])$ – $T_e([\text{O II}])$ relation for the LBT results showed with empty symbols. The solid orange line represents the temperature relation derived by Rogers et al. (2021). The dotted lines in each panel represent the 1:1 relation.

between those temperatures. The LBT and ESI observations follow the relationship derived by Rogers et al. (2021) with some dispersion resulting mainly from the use of the $T_e([\text{N II}])$ results. We stress again that $T_e([\text{N II}])$ are uncertain in the high- T_e /low metallicity limits because $[\text{N II}] \lambda 5755$ is weaker at such metallicities, for that reason we are more confident in $T_e([\text{O II}])$ given the general agreement with the temperature relation presented in Figure 4. Future analysis of such relationships between $T_e([\text{O II}])$ and $T_e([\text{O III}])$ and $T_e([\text{S III}])$ will be presented in K. Z. Arellano-Córdova et al. (in preparation) using CLASSY galaxies, which cover a wider range of physical properties than the local H II regions (Croxall et al. 2016; Arellano-Córdova & Rodríguez 2020; Berg et al. 2020; Rogers et al. 2021). In addition, we will use photoionization models to constrain the temperature relations.

4.2. O/H Abundance

The ionic abundances of O^+ were calculated using the adopted $T_e([\text{O II}])$ or $T_e([\text{N II}])$ representative of the low-ionization zone. To derive O^+ , we use $[\text{O II}] \lambda 3727$ when this line was available and the $[\text{O II}] \lambda \lambda 7320, 7330$ lines for the rest of the observations. For those spectra with both $[\text{O II}] \lambda 3727$ and $\lambda \lambda 7320, 7330$ lines, we compared the results obtained for O^+ . We find an excellent agreement with small differences of 0.02 dex.

For high-ionization ions, O^{2+} , we use $T_e([\text{O III}])$ as representative of such an emitting zone. In Table 4, we list the adopted T_e associated with the low- and high-ionization zones in Columns 8 and 9 ($T_e([\text{O II}])$ (low) and $T_e([\text{O III}])$ (high). In the same Table 4, we also list the ionic abundances of O in Columns 10 and 11.

The total oxygen abundance was calculated by summing the contribution of $\text{O}^+/\text{H}^+ + \text{O}^{2+}/\text{H}^+$. We neglected any contribution of O^{3+}/H^+ to O/H as it is negligible (Berg et al. 2021). The uncertainties were calculated using Monte Carlo simulations by generating 500 random values assuming a Gaussian distribution with sigma associated with the uncertainty. In Table 4, we list the results of $12+\log(\text{O}/\text{H})$ in Column 12 for the whole sample. In addition, in Table 5, we present the results of the metallicity for the multiple apertures in Columns 2–5, and the differences in metallicity, $\Delta\text{O}/\text{H} = \text{O}/\text{H}_{\text{IFU, long-slit}} - \text{O}/\text{H}_{\text{SDSS}}$ in Columns 6–8.

4.3. Ionization Parameter

We define $\text{O}_{32} = [\text{O III}] \lambda 5007 / [\text{O II}] \lambda 3727$ as a proxy of the ionization parameter. We calculate O_{32} for five galaxies of SDSS spectra (J0021+0052, J0808+3948, J1024+0524, J1148+2546, and J1545+0858) and for the whole LBT sample, whose $[\text{O II}] \lambda 3727$ line was available.

For the rest of the sample (ESI and MUSE spectra and some SDSS spectra), we obtained O_{32} using the emissivities of $[\text{O II}] \lambda 3727$ and $[\text{O II}] \lambda \lambda 7320, 7330$ using PyNeb. Such emissivities were calculated using the T_e (low) associated with the low-ionization emitting zone (see Table 8). We derived a representative factor between both $[\text{O II}]$ lines in the red and blue ranges for each galaxy. To estimate the intensity of $[\text{O II}] \lambda 3727_{\text{estimated}}$, we used the observed emission lines of $[\text{O II}] \lambda \lambda 7320, 7330$ multiplied by the factor calculated from the emissivity ratio of $j[\text{O II}] \lambda 3727 / j[\text{O II}] \lambda \lambda 7320, 7330$, for each galaxy. In Table 6, we list the results of O_{32} for our sample of galaxies. We have identified those galaxies of the SDSS sample with estimates of $[\text{O II}] \lambda 3727$ with an asterisk *.

5. Discussion

In this section, we discuss the results implied for the different apertures obtained for CLASSY galaxies in Sections 3 and 4, related to EW, ionization parameter, extinction, SFR, and metallicity.

5.1. Comparison of EWs

We have determined the EWs of $\text{H}\alpha$ and $[\text{O III}] \lambda 5007$ and the ionization parameter for the subsample of 12 CLASSY galaxies. In Table 2, we list the results for the EWs in Columns 7 and 8.

The EWs of $\text{H}\alpha$ range from 68–1620 Å (1.8–3.2 in dex) for SDSS and LBT, and from 280 to 1800 Å (2.4–3.3 in dex), for ESI and MUSE (see Table 2). Such values of EWs are expected in local star-forming galaxies (e.g., Berg et al. 2016; Senchyna et al. 2019). For $\text{EW}([\text{O III}])$, we report values ranging between ~ 7 and 2100 Å (0.8–3.3 in dex) for SDSS and LBT, from ~ 280 –1800 Å (2.4–3.3 in dex) for ESI, and ~ 430 –1500 Å (2.6–3.2 in dex) for MUSE.

In panels (a) and (b) of Figure 5, we show a comparison between the EWs of $[\text{O III}]$ and $\text{H}\alpha$ derived using SDSS spectra and those results using long-slit and IFU spectra of LBT, ESI,

Table 5
Differences in the Metallicity of CLASSY Spectra from Different Apertures

Galaxy	SDSS (3" cir.)	MUSE (2.5" cir.)	LBT (1" slit)	ESI (1" slit)	$\Delta \log O/H$	
J0021+0052	8.22 ± 0.06	8.16 ± 0.09	-0.06	
J0942+3547	8.05 ± 0.03	8.10 ± 0.30		+0.05
J0944-0038	7.81 ± 0.02	...	7.82 ± 0.03	7.73 ± 0.01	+0.01	-0.08
J1024+0524	7.90 ± 0.02	7.55 ± 0.04		-0.35
J1044+0524	7.44 ± 0.02	7.28 ± 0.04	7.44 ± 0.02	...	-0.16	0.00
J1129+2034	8.35 ± 0.04	8.39 ± 0.05		-0.04
J1132+5722	7.42 ± 0.10	7.50 ± 0.13		+0.08
J1148+2546	8.00 ± 0.02	...	7.97 ± 0.02	7.97 ± 0.01	-0.03	-0.03
J1323-0132	7.80 ± 0.17	...	7.74 ± 0.02	...	-0.06	
J1418+2102	7.56 ± 0.02	7.59 ± 0.03	7.60 ± 0.02	...	+0.03	+0.04
J1545+0858	7.74 ± 0.02	...	7.78 ± 0.02	...		-0.03

Note. Metallicity values of $12+\log(O/H)$ measured from the optical spectra of CLASSY galaxies. Columns 2 and 3 list the abundances derived from the 3" and 2.5" circular apertures of the SDSS and MUSE spectra, respectively, and Columns 4 and 5 list the abundances derived from the 1" long-slit apertures of the LBT and ESI spectra, respectively. The differences in O/H between the IFU (MUSE) and long-slit (LBT and ESI) apertures versus the SDSS apertures are represented as $\Delta O/H = O/H_{\text{IFU, long-slit}} - O/H_{\text{SDSS}}$.

Table 6
Differences in the Ionization Parameter of CLASSY Spectra from Different Apertures

Galaxy	SDSS (3" cir.)	MUSE (2.5" cir.)	LBT (1" slit)	ESI (1" slit)	$\Delta \log O_{32}$	
J0021+0052	0.38 ± 0.01 ^a	0.62 ± 0.01 ^a	+0.24	
J0808+3948	-0.27 ± 0.04	...	-0.15 ± 0.06	...		+0.12
J0942+3547	0.56 ± 0.01 ^a	0.36 ± 0.01		+0.20
J0944-0038	0.76 ± 0.01 ^a	...	0.89 ± 0.02	0.57 ± 0.01	+0.13	-0.19
J1024+0524	0.65 ± 0.01	0.65 ± 0.04		0.0
J1044+0353	1.23 ± 0.01 ^a	1.28 ± 0.01 ^a	1.23 ± 0.01	...	+ 0.05	0.00
J1129+2034	0.34 ± 0.01 ^a	0.26 ± 0.02		-0.08
J1132+5722	0.18 ± 0.01 ^a	0.54 ± 0.01		+0.36
J1148+2546	0.64 ± 0.01	...	0.73 ± 0.02	0.64 ± 0.01	+ 0.09	0.0
J1323-0132	1.65 ± 0.01 ^a	...	1.58 ± 0.03	...	-0.07	
J1418+2102	0.96 ± 0.01 ^a	0.98 ± 0.01 ^a	1.03 ± 0.01	...	+0.02	+0.07
J1545+0858	0.84 ± 0.01	...	0.98 ± 0.02	...		+0.14

Notes. The ionization parameter ($O_{32} = [O \text{ III}] \lambda 5007 / [O \text{ II}] \lambda 3727$) measured from the optical spectra of CLASSY galaxies. Columns 2 and 3 list the results of $\log(O_{32})$ derived from the 3" and 2.5" apertures of the SDSS and MUSE spectra, respectively, and Columns 4 and 5 list the results of $\log(O_{32})$ for the 1" apertures of the LBT and ESI spectra, respectively. The differences in $\log(O_{32})$ between the IFU (MUSE) and long-slit (LBT and ESI) apertures versus the SDSS apertures are represented as $\Delta \log O_{32} = O_{32}(\text{IFU, slit}) - O_{32}(\text{SDSS})$.

^a The intensity of $[O \text{ II}] \lambda 3727$ was estimated using the $[O \text{ II}] \lambda \lambda 7320, 7330$ fluxes (see also Section 4.3).

and MUSE. Overall, we find consistent results among the different setups with differences lower than 0.07 dex for $EW(H\alpha)$ with respect to the SDSS $EW(H\alpha)$, except for J1132+5722, which shows a difference of 0.2 dex. However, for $EW([O \text{ III}])$, the differences can reach up to 0.2 dex for the ESI and LBT spectra, and for MUSE the differences can reach up to 0.1 dex with respect to the SDSS $EW([O \text{ III}])$. These differences can be due to the different apertures collecting different relative amounts of nebular emission and stellar continuum.

We have also compared the results of EWs as a function of the fraction of total optical light captured by the different aperture sizes used in these observations. We estimated the total galaxy radius using r -band images from Pan-STARRS following the same procedure as used in Berg et al. (2022) in CLASSY (Paper I). We approximated the total extent of the r -band light, R_{100} , as the radius containing nearly all of the integrated light (although 92.5% was used to avoid unphysical sizes). Because our targets have the majority of their light

contained within a compact center, we define their galaxy sizes as $R_{100}/2$ (see also Figure 1).

Using this value, we estimated the percentage of the light enclosed within the long-slit and IFU apertures as the fraction of the area covered by the respective aperture sizes relative to the adopted optical area of the galaxies: $A_{\text{aper.}}/A_{R_{100}/2}$.

The top panel of Figure 6 shows the SDSS r -band images for a representative sample of our CLASSY galaxies, which show compact and elongated morphologies. The different apertures used in these observations are overplotted as in Figure 1. The dashed circle represents the total galaxy radius, $R_{100}/2$, showing that most of the flux is captured by the IFU and LS apertures. On the other hand, the bottom panel of Figure 6 shows a comparison of the fraction of light ($A_{\text{aper.}}/A_{R_{100}/2}$) covered by different apertures as a function of the EWs of $[O \text{ III}] \lambda 5007$ (a) and $H\alpha$ (b). We have identified the galaxies according to their numbers in Table 1. The same number corresponds to the same galaxy in the different observations. Figure 6 indicates that although the light fraction changes up to

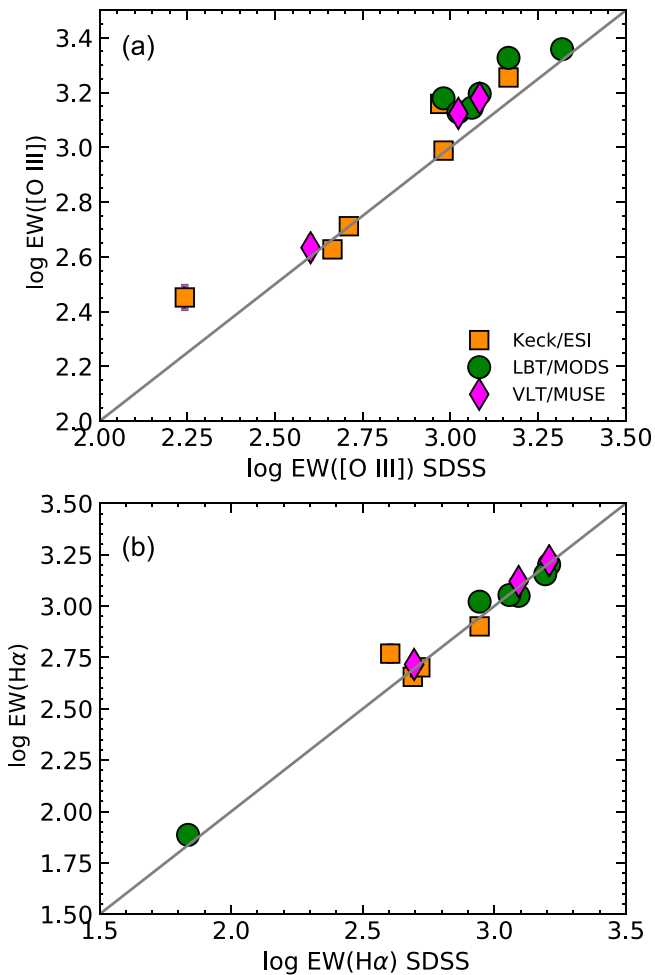


Figure 5. Comparison of log EW of [O III] (a) and H α (b) of the MUSE, LBT, and ESI apertures with respect to SDSS. The solid line represents the 1:1 relationship. The results of the EWs are reported in Table 2.

$\sim 20\%$ between observations of a given galaxy, there is little change in the EWs: the difference in EW is lower than ~ 0.1 dex for most of the galaxies (see, also, Figures 5 and 9). Interestingly, this suggests that the stellar and nebular emissions have similar distributions (e.g., centrally dominant distributions) within these compact galaxies such that aperture differences have little effect on the EW measurements.

We also find that in most galaxies, the percentage of light covered is larger than 60% for apertures of $3''$ and $2''.5$. For long-slit LBT and ESI spectra, the light enclosed within such apertures ranges between 20% and 60%. We also note that for J1129+2034 and J1132+5722, their percentage is lower than 20% for either the IFU ($\sim 30\%$) of long-slit apertures. In fact, those galaxies have an elongated form (see the top panel of Figure 6). However, the observations for those galaxies are where the peak of star formation is located.

5.2. Comparison of Ionization Parameter

We have analyzed the variations of the ionization parameter with aperture size. Overall, we find that differences in $\log(O_{32})$ can reach values of up to ~ 0.14 dex. There are some exceptions with differences larger than 0.2 dex. Note that part of these large differences might be due to the estimate of [O II] $\lambda 3727$ using the [O II] $\lambda\lambda 7320, 7330$ lines. To check this, we compare the values of O_{32} for the galaxies in the SDSS and

LBT samples for which the [O II] $\lambda 3727$ emission lines are available. Such galaxies are J0808+3948, J1148+2546, and J1545+0858. We find that the differences calculated are up to 0.14 dex, except for J1148+2546, which shows a difference of 0.08 dex. In this case, the LBT spectrum provides higher values of O_{32} than the SDSS spectrum. Part of these differences might be due to the sampled region within the galaxy. However, we find the same result for J1148+2546 using the ESI spectrum (see Table 6).

5.3. Comparison of the $E(B - V)$ Values

The results presented in Table 2 provide a broad view of the variations derived using Balmer ratios to calculate the reddening of this sample of star-forming galaxies. In Figure 7, we show the behavior of $H\alpha/H\beta$, $H\gamma/H\beta$, and $H\delta/H\beta$ and the adopted value of $E(B - V)$ for the SDSS, ESI, and LBT apertures. The X-axis shows the 12 galaxies studied here ordered by increasing metallicity. The different symbols indicate the Balmer ratio used to estimate $E(B - V)$ using Equation (1). We discarded the results of MUSE because of the missing coverage of $H\gamma/H\beta$ and $H\delta/H\beta$ for J1044+0353 and J1418+2102.

In general, the SDSS, ESI, and LBT observations show no variation in the distribution of $E(B - V)$ with respect to metallicity for the different estimates of $E(B - V)$ using Balmer lines. The dashed lines in the top panels of Figure 7 indicate the mean values of $E(B - V)$ for each set of observations in color code with the symbols, including the adopted values of $E(B - V)$. Such values, mean, and dispersion for the results of $E(B - V)$ using Balmer ratios are reported in Table 7. Note those estimates of the dispersion of $E(B - V)$ in Table 7 depend on the number of galaxies with measurements of $H\alpha/H\beta$, $H\gamma/H\beta$, and $H\delta/H\alpha$ available in the observed spectra. For the SDSS sample, we find similar values within the uncertainties implied for the different Balmer ratios used.

In Figure 7, it can be observed that the SDSS spectra with an aperture size of $3''$ show less scatter and lower uncertainties in the $E(B - V)$ implied by the different Balmer line ratios in comparison to those obtained using long-slit spectra. In addition, it seems that the LBT results show systematic effects for individual $E(B - V)$ results, but the adopted $E(B - V)$ is consistent with SDSS results.

For LBT spectra, $E(B - V)$ derived using $H\gamma/H\beta$ and $H\delta/H\beta$ show higher values with respect to $H\alpha/H\beta$ in comparison to those of SDSS and ESI. For example, such differences implied in the $E(B - V)$ estimate might be due to stellar continuum subtraction. In the H II regions of local disk galaxies, the discrepancy between $H\alpha/H\beta$ and $H\gamma/H\beta$ and $H\delta/H\beta$ has been reported in different works, implying that this issue is common in other environments (Croxall et al. 2016; Rogers et al. 2021).

On the other hand, some of the results of $E(B - V)$ provide negative reddening calculated for some spectra of SDSS and ESI (see Figure 7 and Table 2), derived using $H\gamma/H\beta$ and $H\delta/H\beta$. Previously, Kewley et al. (2005) found similar behavior for some galaxies in their sample. These authors pointed out as a possible cause the errors in the stellar subtraction, flux calibrations, and uncertain measurements due to noise. However, those values should agree within the errors. We have revised the emission lines fitting in those spectra with negative $E(B - V)$ around $H\gamma$ and $H\delta$. In general, the range in a wavelength where those lines are located shows no apparent

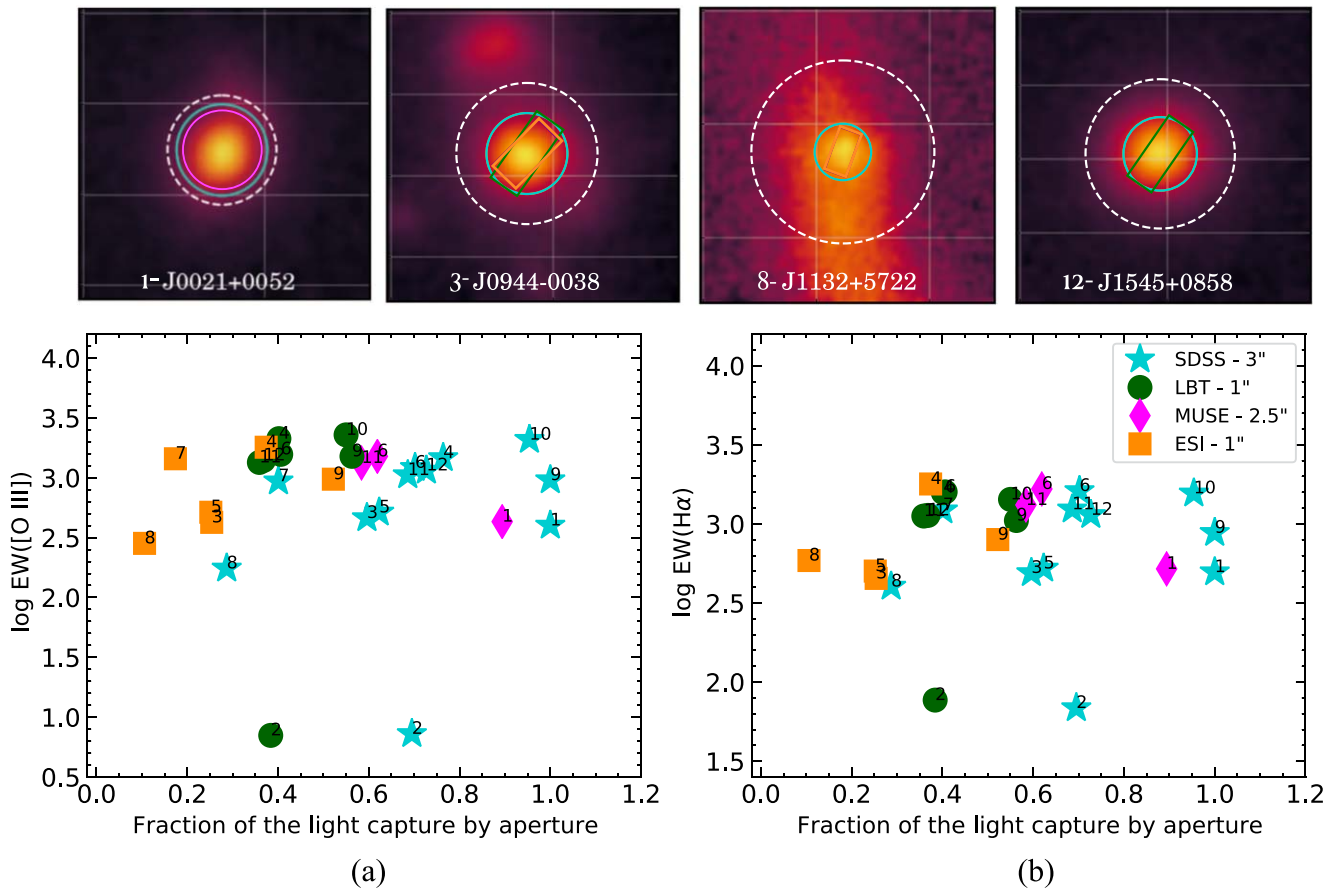


Figure 6. *Top:* SDSS r -band images of the four galaxies of this sample (see also Figure 1). The $2.5''$ MUSE aperture and the $1''$ LBT and ESI apertures are shown as a magenta circle and green and orange boxes, respectively. The $3''$ SDSS aperture is also shown as a cyan circle, and the dotted circle represents the total galaxy radius defined as $R_{100}/2$ (see Table 1 and Section 5.1). *Bottom:* comparison of log EW of [O III] (a) and $H\alpha$ (b) for the SDSS, MUSE, LBT, and ESI apertures vs. the fraction of total optical light enclosed by the respective spectral aperture, $A_{\text{aper}}/A_{R_{100}/2}$. The results of the EWs are reported in Table 2. The numbers identify the ID numbers of the galaxies listed in Table 1.

issues in the flux measurements of those Balmer lines. However, we do not exclude that stellar continuum subtraction might affect the flux measured in those lines as was suggested by Groves et al. (2012). In an incoming paper, we will assess the impact of the reddening correction implied by Balmer and Paschen lines calculating $E(B - V)$ (Rogers et al. 2021; Méndez-Delgado et al. 2021; Aver et al. 2021) using a different set of observations of CLASSY. In particular, the LBT observations of this paper (see Figure 2), which cover a wide range of wavelengths. It allows analyzing in much more detail the reddening correction, dust geometry (Scarlata et al. 2009), the ionization structure of the gas, the electron density and temperature using different diagnostics, chemical abundances of different ions, and the very high-ionization emission lines (Berg et al. 2021).

Now, we show the comparison of different apertures implied in the results of the adopted $E(B - V)$ with respect to the SDSS results, which is shown in Figure 8. The symbols represent the observations implied for the different apertures, and the dashed line indicates the 1:1 relationship. In general, the differences, $\Delta E(B - V) = E(B - V)_{\text{IFU, long-slit}} - E(B - V)_{\text{SDSS}}$ are lower than 0.1 dex for most of the observations (see also Table 2).

Finally, we also compare the reddening derived by averaging the values from three different Balmer line ratios $E(B - V)_{\text{adopted}}$ as a function of [O III] $\lambda 5007$ and $H\alpha$ EWs. In

Figure 9, we show a comparison between the differences between the $E(B - V)$ adopted values and the EWs of [O III] $\lambda 5007$ (a) and $H\alpha$ (b) with respect to the SDSS results. We find that at least for the range implied for this sample, $E(B - V)$ versus EWs seems to be constant. Note that $E(B - V)$ versus $\text{EW}([\text{O III}])$ shows a larger dispersion than $\text{EW}([\text{H}\alpha])$, although for a different number of galaxies (see Table 2). However, the difference between the LS and IFU samples is lower than 0.1 dex for most of the galaxies for either IFU or LS apertures.

5.4. Comparison of Density, Temperature, and Metallicity

Here, we analyze whether the use of different apertures impacts the physical condition and chemical abundance determinations. In principle, both density and temperature diagnostics can be affected by observational problems such as the measurements of faint auroral lines ([O III] $\lambda 4363$ or [N II] $\lambda 5755$), uncertainties involved with extinction and flux calibration, and telluric absorption, among others (Arellano-Córdova & Rodríguez 2020). We have carefully inspected each of the individual spectra implied for the different sets of observations (see also Section 4). It is important to evaluate only the differences indicated for aperture effects.

For density, it was possible to obtain measurements for all the multiple apertures using [S II] intensities (see Table 4 and Section 4). In principle, we use the SDSS observations as a

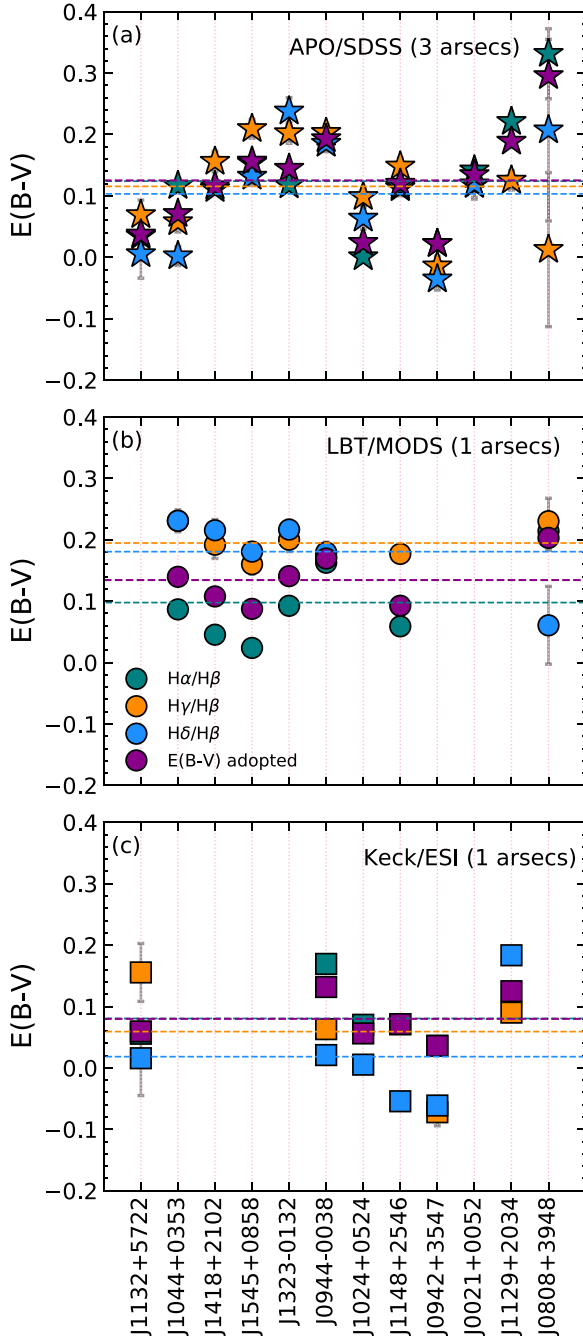


Figure 7. Comparison of the $E(B - V)$ values derived using $H\alpha/H\beta$, $H\gamma/H\beta$, and $H\delta/H\beta$ for the SDSS (a) LBT (b), and ESI (c) spectra, where the symbols represent each instrument, stars, circles, and squares, respectively. The galaxies are ordered at increasing metallicity, see Table 5. The symbols indicate the $E(B - V)$ values derived using the Balmer decrement (teal, orange, and blue) and the final $E(B - V)$ values (purple, see Table 2). The dashed lines represent the mean values of the $E(B - V)$ derived using the Balmer lines and the adopted $E(B - V)$ value for each observation (see Table 7).

comparison sample for our results from the other instruments. The reason is that for SDSS, we can measure most of the physical properties of each galaxy, and because the aperture implied in the SDSS ($3''$) sample maps a similar emission region to that of the HST/COS aperture ($2''.5$). For the SDSS sample, we obtain densities of $50 < n_e \text{ (cm}^{-3}\text{)} < 1100$. J0808+3948, J1044+0353, and J1323-0132 show high values of $n_e > 300 \text{ cm}^{-3}$ in comparison to the rest of the sample. In panel

Table 7
Mean and Dispersion Values of $E(B - V)$ Using the Balmer Decrement for the Different Apertures

$E(B - V)$	SDSS	ESI	LBT
$H\alpha/H\beta$	0.124 ± 0.094	0.080 ± 0.052	0.098 ± 0.067
$H\gamma/H\beta$	0.116 ± 0.074	0.059 ± 0.095	0.195 ± 0.027
$H\delta/H\beta$	0.103 ± 0.093	0.018 ± 0.088	0.181 ± 0.062
$E(B - V)$	0.125 ± 0.080	0.080 ± 0.039	0.134 ± 0.042

Note. The mean and dispersion values of each Balmer ratio correspond to the total number of galaxies of each sample, and those are represented in Figure 7. The $E(B - V)$ shows the mean and dispersion value for the whole sample of observations in each instrument, SDSS, LBT, and ESI.

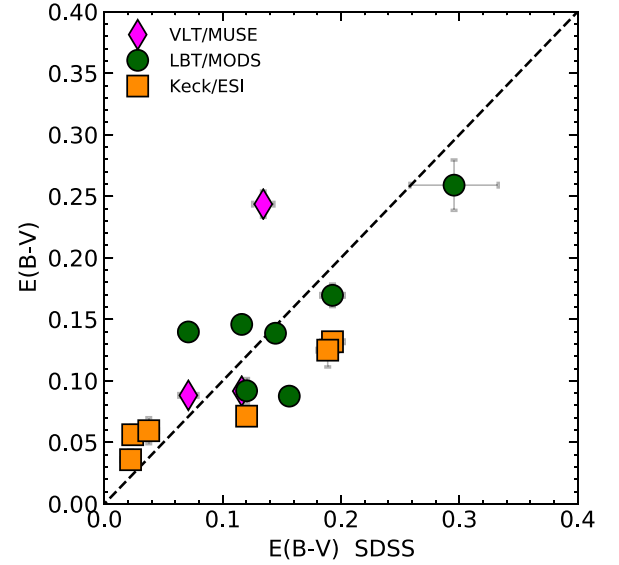


Figure 8. Comparison of the final $E(B - V)$ values derived from the MUSE, ESI, and LBT spectra with the SDSS sample. The symbols indicate the different observations, IFU (VLT/MUSE) and long-slit (Keck/ESI and LBT/MODS) with respect to the APO/SDSS sample. The dashed line represents the 1:1 relationship.

(a) of Figure 10, we show a comparison of the results for $n_e < 300$ using SDSS spectra versus the densities calculated using multiple spectra (we discard the high-density values for display purposes corresponding to J0808+3849 and J1323-0132). We find that at low density, $n_e < 150 \text{ cm}^{-3}$, where more of the CLASSY galaxies are located, long-slit observations show consistent results within the uncertainties with the SDSS sample. For J0808+3948 and J1044+0353, with high-density values, the LBT and SDSS observations show small differences of 40 and 100 cm^{-3} , respectively.

In our first analysis of the electron density for J1323-0132 of LBT, we find a difference of 370 cm^{-3} in comparison to the SDSS aperture. We note that the observed wavelengths of the [S II] lines in J1323-0132 are affected by telluric absorption. We fitted those lines again, taking into account the absorption feature. For J1323-0132, we calculate a new value of $n_e = 640_{-500}^{+800} \text{ cm}^{-3}$, which implies a difference of 50 cm^{-3} with respect to the previous contaminated value. In Table 8, we show the differences in the density, temperature, and metallicities of the IFU and LS apertures concerning the SDSS measurements. Those galaxies with multiple apertures using IFU and LS are also indicated in Table 8 for comparison (J1044+0353 and J1418+2102). In general, we find that the $n_e[\text{S II}]$

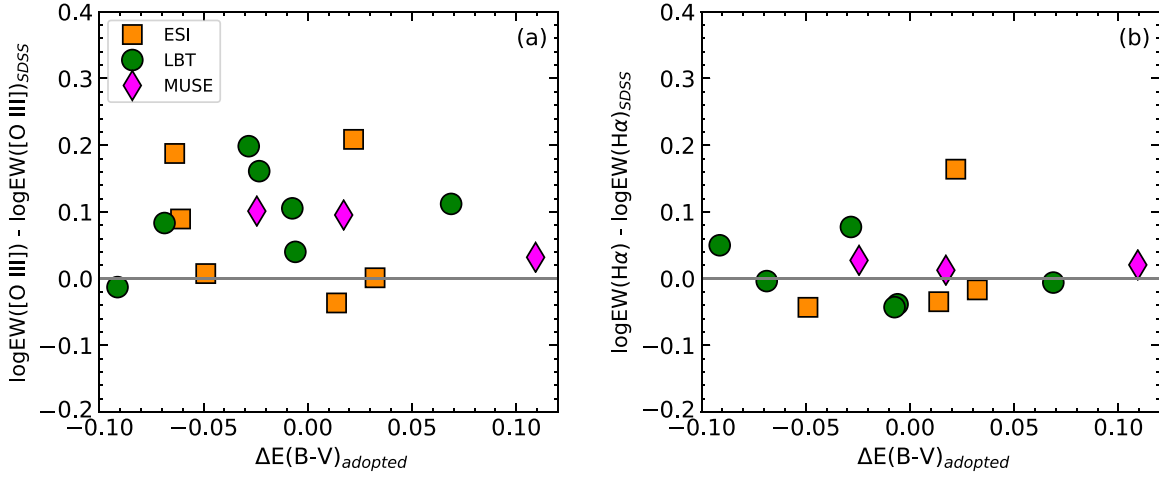


Figure 9. Color-excess differences, $\Delta E(B - V)_{\text{adopted}} = E(B - V)_{\text{IFU,LS}} - E(B - V)_{\text{SDSS}}$ as a function of the adopted EW differences with respect to the SDSS results for [O III] $\lambda 5007$ (a) and H α (b). The symbols show the IFU (VLT/MUSE) and LS (LBT/MODS, Keck/ESI) observations, respectively. Note that the results for the EWs (H α) correspond to those spectra with measurements of H α (see Table 2).

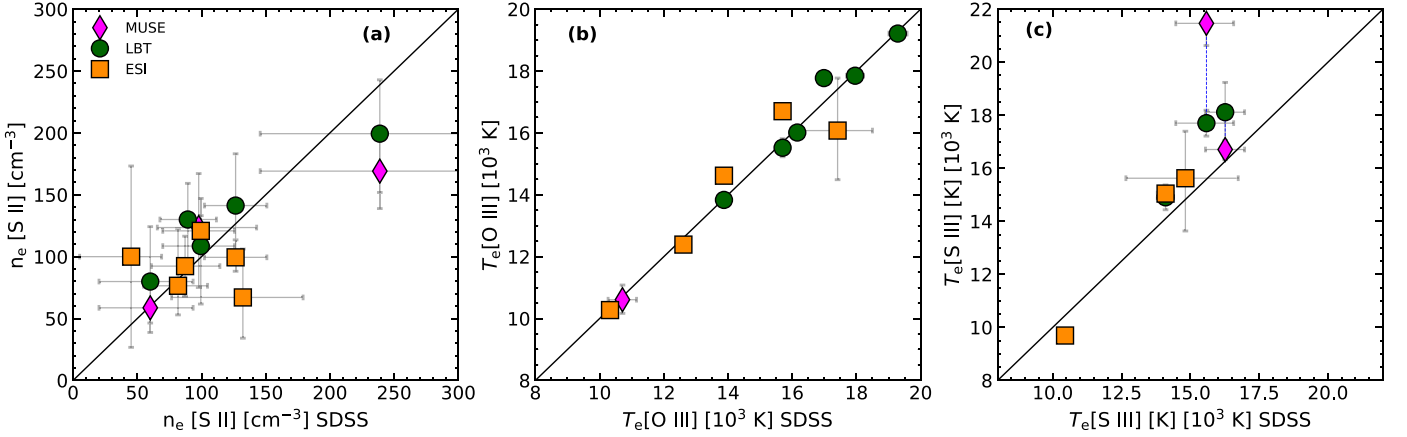


Figure 10. Electron density and temperature for the multiple apertures of CLASSY galaxies. (a) Electron density, $n_e[\text{S II}]$ comparison for the multiple observations. (b) Comparison of $T_e([\text{O III}])$ from the SDSS spectra vs. $T_e([\text{O III}])$ using multiple aperture spectra of MUSE, LBT, and ESI. We discard those galaxies with high density, J0808, and J1323, to better compare those with low density. (c) $T_e([\text{S III}])$ calculated using SDSS spectra in comparison with $T_e([\text{S III}])$ calculated using multiple aperture spectra. The dotted line joins the same galaxy from the MUSE and LBT data with a large difference in both the SDSS and LBT data. The solid lines indicate the 1:1 relation. The different symbols correspond to the multiple apertures, which are labeled in the top of the left panel.

Table 8
Difference in Electron Density, Temperature, and Metallicities with Respect to the SDSS Sample

	J0021+0052 IFU	J0808+3948 LS	J0942+3547 LS	J0944-0038 LS	J1024+0524 LS	J1044+0353 IFU LS
$\Delta n_e[\text{S II}] [\text{cm}^{-3}]$	+30	-100	-50	+20	+20	-70 -40
$\Delta T_e[\text{S III}] [\text{K}]$	N/A	N/A	N/A	-900	N/A	+6100 +2300
$\Delta T_e[\text{O III}] [\text{K}]$	-200	N/A	-200	-1000	N/A	0
	J1129+2034 LS	J1132+5722 LS	J1148+2546 LS	J1323-0132 LS	J1418+2102 IFU LS	J1548+0858 LS
$\Delta n_e[\text{S II}] [\text{cm}^{-3}]$	+10	-80	+10	-50	-10 +20	+40
$\Delta T_e[\text{S III}] [\text{K}]$	-100	-700	N/A	N/A	+500 -1300	N/A
$\Delta T_e[\text{O III}] [\text{K}]$	+200	-1500	+100	+700	N/A -100	-200

Note. Differences in the physical conditions and metallicities of the IFU and LS results respect to the SDSS results. The temperature diagnostics are not available for J0808+3948 for the SDSS spectrum. LS = long slit.

implied for the different apertures are in good agreement with the results of the SDSS aperture with differences lower than 100 cm^{-3} .

On the other hand, we calculated $n_e[\text{O II}] \text{ cm}^{-3}$ for some galaxies. This includes the whole sample of the LBT observations and four galaxies of SDSS (J0021+0052, J1024+0524, J1044+0353, and J1548+0858, see also Table 4).

First, we compare the results between the density diagnostics of $n_e[\text{O II}]$ and $n_e[\text{S II}]$ derived for the LBT spectra. Overall, we find differences lower than 100 cm^{-3} for most of the LBT sample. The exception is J0021+0052 and J0808+3948 whose difference is up to 470 cm^{-3} . In a similar way, the four galaxies with $n_e[\text{O II}]$ show differences of up to $\sim 210 \text{ cm}^{-3}$. Note that the density diagnostic of $n_e[\text{O II}]$ provides values higher than the results implied by $n_e[\text{S II}]$ in both samples. Next, we compare the results implied by $n_e[\text{O II}]$ for two galaxies in common in the LBT and SDSS samples (J1148+2546 and J1548+0858). We find differences lower than 80 cm^{-3} .

Concerning the electron temperature, we have calculated $T_e([\text{O III}])$ and $T_e([\text{S III}])$ for most of the spectra of the CLASSY galaxies (see Table 4). $T_e([\text{O III}])$ was measured in the whole SDSS sample (with the exception of J0808+3948) and in some galaxies for the rest of the observations with different apertures. In panel (b) of Figure 10, we show a comparison of the $T_e([\text{O III}])$ results for the multiple apertures. In general, $T_e([\text{O III}])$ for the IFU and long-slit apertures are consistent with the SDSS results with differences lower than 700 K for most of the objects (see Table 8). J1132+5722 of the ESI sample shows a difference of -1500 K in $T_e([\text{O III}])$ with respect to the SDSS measurements. This large discrepancy might be related to the measurement of $[\text{O III}] \lambda 4363$ or due to spatial variations. Note that our comparison to the SDSS results is due to the analysis of the variations of the physical properties in each galaxy with respect to other apertures. Therefore, it does not imply that the temperatures or the different physical conditions of the SDSS sample are the true values since they might also be affected by different biases (i.e., observational problems). For the objects with $S/N([\text{S III}]) > 3$, we computed $T_e([\text{S III}])$ implied by the SDSS, LBT, ESI, and MUSE apertures. We find that $T_e([\text{S III}])$ calculated using the MUSE spectra provides higher temperatures with respect to the SDSS results (see Table 8). In particular, J1044+0353 shows a difference of up to 6100 K with respect to $T_e([\text{S III}])$ implied by the SDSS and LBT spectra. In fact, $T_e([\text{S III}])$ derived using LBT also shows a higher value than SDSS. In panel (c) of Figure 10, we show a comparison between $T_e([\text{S III}])$ derived using the SDSS sample and IFU and long-slit apertures. In that figure, the results using MUSE and LBT for J1044+0353 are represented by a rhomboid and circle, which are joined by a dotted line. We find that the difference between these two measurements and the results of SDSS is up to 6100 K (see Table 8). These discrepancies might be due to telluric absorption affecting $[\text{S III}] \lambda 9069$, the only line available in the MUSE spectra. In general, we find differences in $T_e([\text{S III}])$ lower than 800 K.

Since metallicity is an important measure in star-forming galaxies, we analyze the impact to use multiple aperture sizes for the same galaxy in the computation of metallicity. One of the main advantages of the sample of CLASSY galaxies studied here is the availability of measurements of electron temperature, which allows a better constraint on the estimated chemical abundance determinations. In Figure 11, we show a comparison between the metallicities calculated by the different apertures and those by the SDSS aperture. Long-slit spectra correspond to the squares and circles, while the rhomboids correspond to an aperture similar to SDSS and HST/COS. In general, our results show that LS apertures (most of the samples have aperture sizes of $\approx 1'' \times 2''$) are consistent with the results implied by the $3''$ aperture of the SDSS sample

within the uncertainties with differences generally lower than 0.08 dex.

However, we find a difference in metallicity in using the ESI spectra. Such discrepancies are mainly related to the larger differences that we found for $T_e([\text{O III}])$ (see Table 8).

In principle, it is expected that the results obtained from MUSE agree with those of SDSS given that the apertures map similar emissions. For the three galaxies with MUSE observations, J0021+0052, J1044+0353, and J1148+2546, we find differences in metallicity lower than 0.06 dex, with the exception of J1044+0353 with a difference of 0.16 dex (see Table 8). The reason for this difference might be due to the estimate of $T_e([\text{O III}])$ by the temperature relation in Equation (3). J1044+0353 is an extremely high-ionization galaxy showing a large amount of high-ionization species (Berg et al. 2021). In the total oxygen abundance, the dominant ion is O^{++} , implying a strong dependence of the estimated value of $T_e([\text{O III}])$ from $T_e([\text{S III}])$. Therefore, again another possible explanation for this difference might be associated with observational problems related to the telluric lines affecting the strength of $[\text{S III}] \lambda 9069$ and/or $[\text{S III}] \lambda 9532$. After a visual inspection of this sample, we discard such contamination by the underlying absorption lines.

In summary, we find a good agreement between the IFU and LS apertures for the different physical properties derived for this sample of CLASSY galaxies. The galaxies studied here are mainly dominated by a single bright star formation cluster. Therefore, it is expected that such differences will be minimal. Another point is that despite instrumental effects and systematic differences between instruments, we are getting the same results.

On the other hand, since the computation of T_e depends on the T_e diagnostic available in the emission spectra of each galaxy, it is important to have a reliable constraint of the temperature and ionization structure of the nebular gas. Therefore, this analysis supports comparing the physical properties obtained using optical data with those results used to constrain UV analysis for the apertures of different sizes with similar characteristics to the CLASSY sample (M. Mingozzi et al. in preparation).

5.5. Aperture Analysis Using MUSE

As an additional analysis, we have taken advantage of the integrated spectra obtained from MUSE using different aperture sizes for J0021+0052, J1044+0353, and J1418+2102. This new set of spectra comprises sizes between $1''.0$ and $7''.5$ in diameter with steps of $0''.5$. We analyzed the variations of $E(B-V)$, n_e , T_e , ionization parameter, metallicities, SFR, and EWs as a result of the different aperture sizes derived from MUSE.

We have calculated the SFR using the $\text{H}\alpha$ flux measurements obtained in each MUSE aperture. We use the $E(B-V)$ adopted values in each aperture to correct $\text{H}\alpha$ fluxes for extinction. The luminosity distances were taken from Berg et al. (2022, see their Table 5), which consider peculiar motions due to the low redshift of the CLASSY galaxies. To estimate the SFR, we use the expression reported by Kennicutt & Evans (2012): $\log \text{SFR}(L(\text{H}\alpha)) = \log L(\text{H}\alpha) - 41.27$. This expression is based on updated stellar models and initial mass function fit by Chabrier (2003) (mass range $0.1-100 M_\odot$). SFR uncertainties were calculated using error propagation.

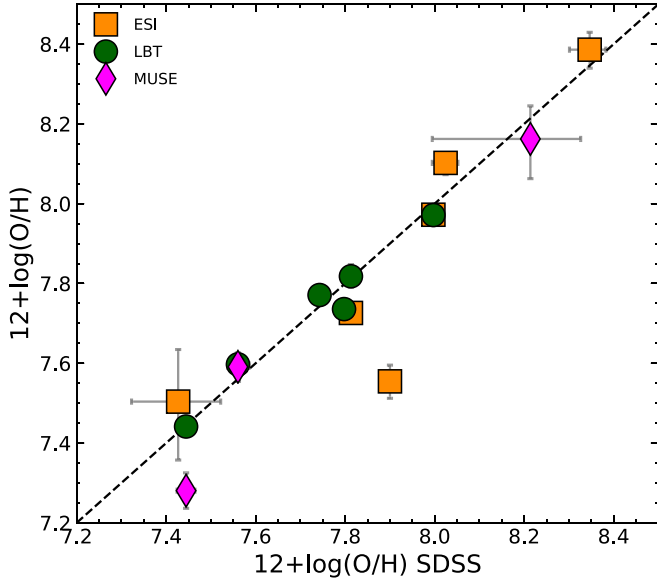


Figure 11. Metallicity comparison between the results implied by the SDSS sample and the multiple apertures of IFU and LS (LBT and ESI). The differences in O/H are shown in Table 5 for the LS and IFU results with respect to SDSS.

In Figure 12, we show the results for the integrated MUSE spectra using a different aperture size. The triangles, circles, and squares represent J0021+0052, J1044+0353, and J1418+2102, respectively. For comparison, we have added the results derived from the SDSS spectra, which are shown in each panel of Figure 12 with empty stars with the same color as their respective galaxy. The two vertical bars represent the aperture size of HST/COS and SDSS of $2''.5$ and $3''.0$, respectively. Overall, Figure 12 shows that the variations in the galaxy properties convergent at an aperture size of $4''$, implying that most of the flux can be in-closed at aperture sizes similar to those of the SDSS ($3''$) and COS ($2''.5$) apertures for these galaxies. In panels (a)–(e), we compared each individual spectrum as a function of the extinction, the physical conditions (n_e and T_e), and metallicity. In general, we find consistent results through the multiple aperture sizes. We note that for J0021+0052 the extinction calculated using $H\alpha/H\beta$ shows a difference of 0.15 dex when the $1''.0$ and $3''.0$ apertures are compared, increasing such difference as the apertures become bigger. However, we find a smooth variation in $E(B - V)$ for J10144+0353 and J1418+2102 with respect to the different aperture sizes. We also calculated $E(B - V)$ using $H\gamma/H\beta$ for J0021+0052 (see the blue triangles in panel (a) of Figure 12.), showing a similar behavior in comparison to the other two

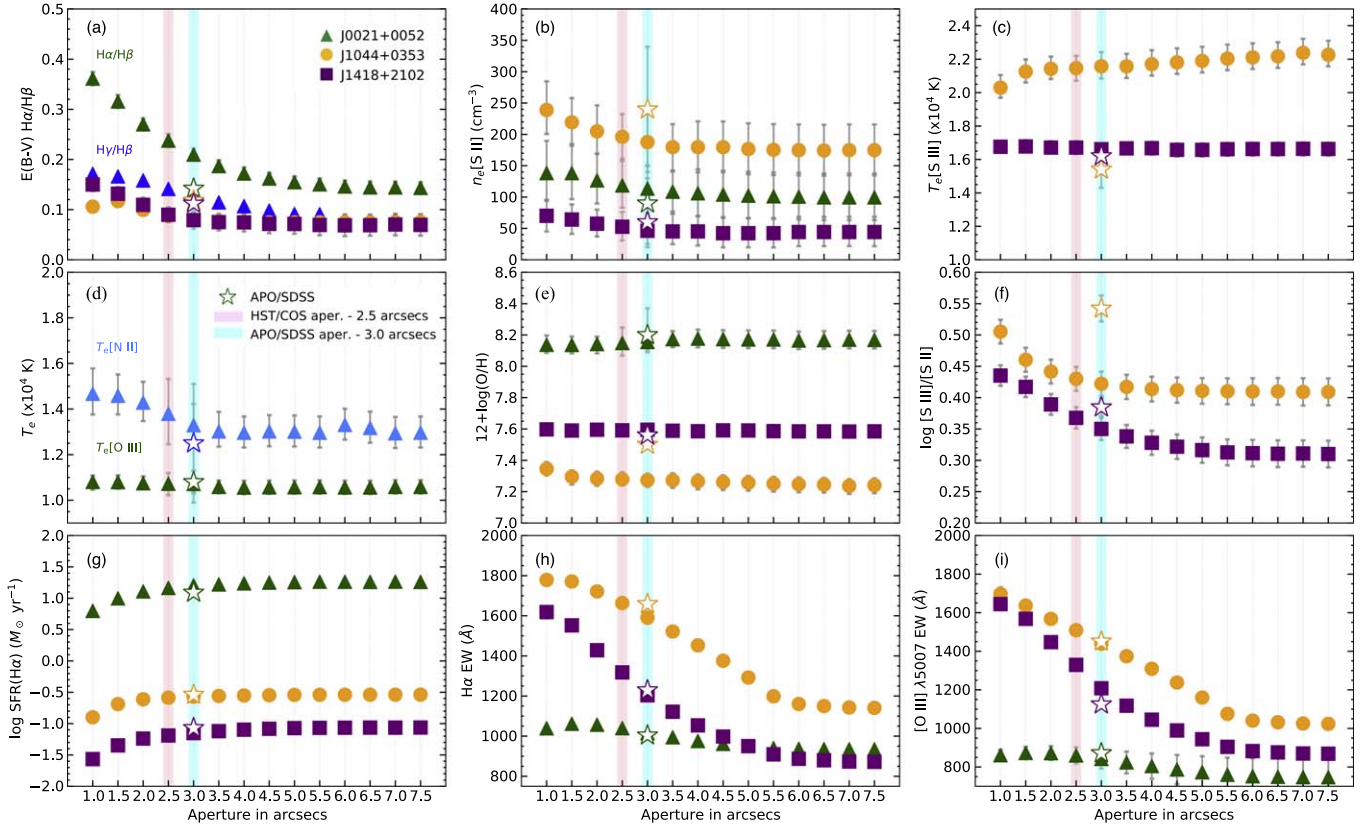


Figure 12. MUSE IFU aperture variations. Integrated MUSE spectra using aperture sizes from $1''.0$ – $7''.5$ in diameter in steps of $0''.5$ for J0021+0052, J1044+0353, and J1418+2102. The different symbols indicate the results for J0021+0052 (triangles), J1044+0353 (circles), and J1418+2102 (squares). For comparison, we added the results using the SDSS aperture of the $3''.0$ (stars and cyan bar) spectra for those galaxies. We identify the aperture size of HST/COS of $2''.5$ (pink bar). Panel (a) shows the reddening derived using $H\alpha/H\beta$ and $H\gamma/H\beta$ (only for J0021+0052 in blue triangles). Panels (b)–(e) show the variation in electron density (n_e), electron temperature ($T_e[\text{O III}]$, $T_e[\text{N II}]$, and $T_e[\text{S III}]$), and metallicity. Note that in panels (c) and (d), $T_e[\text{S III}]$ was calculated only for J1044+0353 and J1418+2102, and $T_e[\text{O III}]$ and $T_e[\text{N II}]$ were only determined for J0021+0052, respectively. Panel (f) shows a proxy of the ionization parameter measured as $[\text{S III}](\lambda 9069 + \lambda 9532)/(\lambda 6717 + \lambda 6731)$ representative of the low-ionization emitting zone (see, e.g., Berg et al. 2021). Panels (g)–(i) represent the results of the SFR, and the EWs of $H\alpha$ and $[\text{O III}]$, respectively. The results of the EW($H\alpha$) and EW($[\text{O III}]$) for the MUSE and SDSS results for J0021+2102 are multiplied by a factor of 2 for display purposes. Note that J0021+2102 shows a smooth variation along the different apertures. The results show that the physical conditions, metallicity, and physical properties converge to constant values at aperture sizes of $\sim 4.0''$ in diameter.

Table 9
Dereddened Emission Line Intensities for the APO/SDSS Spectra for 12 CLASSY Galaxies

Wavelength (Å)	Ion	J0021+0052	J0808+3948	J0942+3547	J0944-0038	J1024+0542	J1044+0352
3726.04	[O II]	87.0 ± 3.1	103.49 ± 9.0	50.8 ± 1.6	...
3728.80	[O II]	102.6 ± 3.2	65.8 ± 1.7	...
4101.71	H δ	26.29 ± 0.51	27.67 ± 3.14	27.35 ± 0.41	26.45 ± 0.33	25.41 ± 0.35	27.82 ± 0.37
4340.44	H γ	47.33 ± 0.57	54.71 ± 3.7	48.06 ± 0.44	47.13 ± 0.42	45.42 ± 0.36	47.8 ± 0.46
4363.21	[O III]	3.76 ± 0.48	...	6.8 ± 0.29	11.86 ± 0.24	9.15 ± 0.29	13.7 ± 0.29
4861.35	H β	100.0 ± 1.0	100.0 ± 5.0	100.0 ± 1.0	100.0 ± 1.0	100.0 ± 0.76	100.0 ± 1.0
4958.61	[O III]	151.23 ± 2.25	18.09 ± 2.19	169.03 ± 1.75	185.89 ± 2.33	173.17 ± 1.73	147.66 ± 2.79
5006.84	[O III]	455.26 ± 4.05	55.33 ± 2.91	497.56 ± 3.94	555.47 ± 3.96	520.04 ± 3.33	...
5754.64	[N II]	0.57 ± 0.24	...	0.48 ± 0.21
6312.06	[S III]	1.04 ± 0.15	...	1.77 ± 0.13	1.46 ± 0.04	1.72 ± 0.1	0.69 ± 0.07
6562.79	H α	287.2 ± 3.76	296.0 ± 16.1	281.53 ± 3.05	...	273.66 ± 2.39	288.6 ± 4.0
6583.45	[N II]	23.52 ± 2.01	207.7 ± 11.84	10.96 ± 0.89	3.37 ± 4.57	5.96 ± 1.1	0.93 ± 2.49
6716.44	[S II]	16.68 ± 0.37	19.18 ± 1.4	16.43 ± 0.24	7.39 ± 0.1	11.44 ± 0.16	2.42 ± 0.08
6730.82	[S II]	12.64 ± 0.35	24.61 ± 1.64	11.91 ± 0.21	5.74 ± 0.09	8.56 ± 0.15	2.02 ± 0.08
7319.92	[O II]	2.22 ± 0.14	...	1.63 ± 0.13	1.61 ± 0.04	1.69 ± 0.11	0.53 ± 0.06
7339.79	[O II]	1.98 ± 0.14	...	1.46 ± 0.13	1.29 ± 0.04	1.42 ± 0.11	0.49 ± 0.06
9068.60	[S III]	10.94 ± 0.32	...	4.47 ± 0.23
$E(B - V)$		0.135 ± 0.009	0.296 ± 0.036	0.021 ± 0.006	0.193 ± 0.009	0.025 ± 0.006	0.072 ± 0.008
$F_{H\beta}$		292.7 ± 2.2	47.7 ± 1.7	214.5 ± 1.6	813.5 ± 4.7	331.9 ± 1.8	471.9 ± 3.4
Wavelength (Å)	Ion	J1129+2034	J1132+5722	J1148+2546	J1323-0132	J1418+2546	J1545+0858
3726.04	[O II]	59.4 ± 1.4	35.5 ± 1.5
3728.80	[O II]	78.9 ± 1.5	43.1 ± 1.5
4101.71	H δ	...	26.98 ± 0.81	26.26 ± 0.34	24.51 ± 0.45	...	26.79 ± 0.31
4340.44	H γ	48.55 ± 0.45	46.64 ± 0.61	46.52 ± 0.36	45.97 ± 0.45	46.5 ± 0.41	46.09 ± 0.38
4363.21	[O III]	3.4 ± 0.21	5.36 ± 0.72	9.91 ± 0.21	19.17 ± 0.35	12.78 ± 0.39	12.49 ± 0.34
4861.35	H β	100.0 ± 1.07	100.0 ± 1.05	100.0 ± 0.91	100.0 ± 1.15	100.0 ± 0.61	100.0 ± 0.64
4958.61	[O III]	156.54 ± 3.88	69.7 ± 1.02	200.24 ± 2.66	250.37 ± 5.39	155.82 ± 1.33	183.87 ± 1.35
5006.84	[O III]	...	202.24 ± 1.82	607.25 ± 4.76	761.02 ± 8.07	452.0 ± 2.5	543.64 ± 2.84
6312.06	[S III]	1.6 ± 0.05	0.99 ± 0.23	1.32 ± 0.09	...	1.02 ± 0.07	1.22 ± 0.06
6562.79	H α	293.49 ± 3.97	276.18 ± 3.3	278.38 ± 2.59	269.53 ± 3.05	275.16 ± 2.13	277.05 ± 1.86
6583.45	[N II]	11.61 ± 2.11	4.13 ± 1.4	6.26 ± 0.88	1.01 ± 0.86	2.04 ± 0.96	3.2 ± 0.62
6716.44	[S II]	14.9 ± 0.27	12.74 ± 0.3	11.79 ± 0.17	2.11 ± 0.17	5.02 ± 0.09	6.19 ± 0.08
6730.82	[S II]	11.2 ± 0.24	9.94 ± 0.29	8.98 ± 0.15	2.2 ± 0.17	3.66 ± 0.08	4.67 ± 0.07
7319.92	[O II]	2.11 ± 0.06	2.38 ± 0.26	1.76 ± 0.09	0.43 ± 0.07	0.95 ± 0.06	0.94 ± 0.06
7339.79	[O II]	1.7 ± 0.06	2.19 ± 0.25	1.54 ± 0.08	0.4 ± 0.05	0.67 ± 0.06	0.85 ± 0.06
9068.60	[S III]	21.36 ± 0.6	6.73 ± 0.28	6.06 ± 0.23	...
$E(B - V)$		0.191 ± 0.009	0.038 ± 0.008	0.119 ± 0.006	0.147 ± 0.007	0.116 ± 0.005	0.156 ± 0.004
$F_{H\beta}$		386.3 ± 2.9	86.5 ± 0.6	380.0 ± 2.4	168.5 ± 1.4	270.0 ± 1.2	555.3 ± 2.5

Note. Intensity ratios are reported with respect to $I(H\beta) = 100$, where the observed $H\beta$ fluxes (in units of 10^{-16} erg s^{-1} cm^{-2}) are reported in the second to last row. The color-excess values, $E(B - V)$, used to redden the line ratios are listed in the last row.

galaxies in this analysis. In fact, the results for SDSS show a good agreement with those obtained using a $2''.5$ aperture size.

We also find that the electron density and temperature, and metallicity show slight variations in their results for the different aperture sizes (see panels (b)–(e) of Figure 12). For J1044+0353 and J1418+2102, the only temperature diagnostic available is $T_e([S III])$, whose results are in excellent agreement with the rest of the MUSE aperture sizes implied in this analysis. For J1044+0353, the result for $T_e([S III])$ shows a large difference between the MUSE and SDSS data (see Table 8). In Section 5.4, we stress that such a difference could be due attributed to the telluric features affecting the $[S III]$ $\lambda 9069$ emission line.

In Panel (d) of Figure 12, we show the results for $T_e([O III])$ and $T_e([N II])$ for J0021+0052. The results for $T_e([O III])$ are consistent between the different apertures. However, the variation of $T_e([N II])$ is slightly larger, increasing to small aperture sizes. Interestingly, we have calculated high values of

$T_e([N II])$ with respect to those obtained for $T_e([O III])$. On the other hand, panel (e) shows small variations in metallicity as the aperture size increases. Moreover, the SDSS spectra show good agreement with the values of O/H derived either using an aperture of $2''.5$ or $3''.0$. In panel (f) of Figure 12, we compare the variations in the ionization parameter measured as a proxy of $S3S2 = [S III](\lambda 9069 + \lambda 9532)/[S II](\lambda 6717 + \lambda 6731)$ (see, e.g., Berg et al. 2021; Mingozi et al. 2020), which trace the low-ionization emitting zone of the nebula. We used this approach because $[S II]$ and $[S III]$ are directly available for J1044+0353 and J1418+2102 in the MUSE spectra. We find that $\log(S3S2)$ decreases until it reaches a convergence when the aperture size is also $\sim 4''$ in diameter. For J1418+0858, we find a small difference between the MUSE and SDSS results of 0.03 dex for an aperture size of $3''$. However, the $\log(S3S2)$ obtained with MUSE shows a large difference with respect to the SDSS value (see also panel (c) in Figure 12), probably

Table 10
Dereddened Emission Line Intensities Measured for the Keck/ESI Spectra for Five CLASSY Galaxies

Wavelength (Å)	Ion	J0942+3547	J0944-0038	J1024+0524	J1129+2034	J1132+5722	J1148+2546
4101.71	H δ	27.96 \pm 0.29	28.65 \pm 0.16	27.33 \pm 0.37	24.92 \pm 0.46	27.24 \pm 1.26	28.83 \pm 0.2
4340.44	H γ	50.6 \pm 0.4	49.13 \pm 0.21	...	47.94 \pm 0.57	45.02 \pm 1.18	0.0 \pm 0.0
4363.21	[O III]	6.22 \pm 0.24	13.14 \pm 0.13	13.82 \pm 0.38	3.41 \pm 0.23	5.11 \pm 1.0	10.62 \pm 0.22
4861.35	H β	100.0 \pm 0.64	100.0 \pm 0.32	100.0 \pm 1.09	100.0 \pm 0.59	100.0 \pm 1.5	100.0 \pm 0.49
4958.61	[O III]	166.42 \pm 1.65	190.59 \pm 1.45	182.73 \pm 2.4	158.29 \pm 6.23	77.39 \pm 1.53	215.2 \pm 1.36
5754.64	[N II]	0.17 \pm 0.05	0.07 \pm 0.02	0.14 \pm 0.04	0.21 \pm 0.03	0.26 \pm 0.14	0.1 \pm 0.03
6312.06	[S III]	1.82 \pm 0.08	1.52 \pm 0.02	1.51 \pm 0.05	1.86 \pm 0.04	0.88 \pm 0.15	1.27 \pm 0.03
6562.79	H α	282.22 \pm 2.3	287.67 \pm 1.18	281.83 \pm 3.24	...	277.04 \pm 4.19	279.95 \pm 1.6
6583.45	[N II]	11.23 \pm 0.99	3.44 \pm 0.63	5.55 \pm 1.12	13.91 \pm 0.56	3.74 \pm 0.55	5.42 \pm 0.57
6716.44	[S II]	17.77 \pm 0.21	8.12 \pm 0.05	11.48 \pm 0.37	18.43 \pm 0.29	12.82 \pm 0.26	11.12 \pm 0.1
6730.82	[S II]	12.49 \pm 0.19	6.18 \pm 0.05	8.2 \pm 0.36	13.96 \pm 0.23	9.32 \pm 0.21	8.65 \pm 0.09
7319.92	[O II]	2.16 \pm 0.15	1.69 \pm 0.02	1.71 \pm 0.34	2.63 \pm 0.06	1.91 \pm 0.15	1.48 \pm 0.08
7339.79	[O II]	1.75 \pm 0.15	1.3 \pm 0.02	1.36 \pm 0.34	2.06 \pm 0.05	1.5 \pm 0.14	1.39 \pm 0.08
9068.60	[S III]	18.81 \pm 0.27	10.24 \pm 0.12	7.47 \pm 0.2	29.75 \pm 0.81	5.53 \pm 0.16	9.52 \pm 0.12
$E(B - V)$		0.036 \pm 0.008	0.134 \pm 0.003	0.055 \pm 0.008	0.125 \pm 0.013	0.054 \pm 0.010	0.071 \pm 0.004
$F_{H\beta}$		195.8 \pm 1.4	1073.6 \pm 2.4	309.5 \pm 2.4	552.0 \pm 2.3	686.7 \pm 7.3	357.8 \pm 1.2

Note. Intensity ratios are reported with respect to $I(H\beta) = 100$, where the observed H β fluxes (in units of 10^{-16} erg s $^{-1}$ cm $^{-2}$) are reported in the second to last row. The color-excess values, $E(B - V)$, used to reddening correct the line ratios are listed in the last row.

Table 11
Dereddened Emission Line Intensities Measured for the VLT/MUSE Spectra for Three CLASSY Galaxies

Wavelength (Å)	Ion	J021+0052	J1044+0353	J1418+2102
4340.44	H γ	46.36 \pm 0.64
4363.21	[O III]	3.44 \pm 0.47
4861.35	H β	100.0 \pm 1.13	100.0 \pm 1.0	100.0 \pm 1.0
4958.61	[O III]	146.75 \pm 2.27	147.43 \pm 1.16	160.58 \pm 1.86
5006.84	[O III]	440.14 \pm 4.21	436.24 \pm 2.39	470.51 \pm 3.08
5754.64	[N II]	0.67 \pm 0.11
6312.06	[S III]	1.25 \pm 0.09	0.76 \pm 0.01	1.01 \pm 0.02
6562.79	H α	283.54 \pm 4.69	273.4 \pm 2.5	277.26 \pm 2.29
6583.45	[N II]	21.74 \pm 2.21	0.91 \pm 0.091	1.91 \pm 0.69
6716.44	[S II]	16.2 \pm 0.37	2.34 \pm 0.04	5.12 \pm 0.06
6730.82	[S II]	12.56 \pm 0.34	1.9 \pm 0.04	3.74 \pm 0.06
7319.92	[O II]	2.05 \pm 0.07	0.59 \pm 0.01	0.9 \pm 0.02
7339.79	[O II]	1.72 \pm 0.06	0.49 \pm 0.01	0.79 \pm 0.02
9068.60	[S III]	...	3.15 \pm 0.16	5.78 \pm 0.2
$E(B - V)$		0.214 \pm 0.011	0.088 \pm 0.007	0.091 \pm 0.006
$F_{H\beta}$		187.0 \pm 1.5	404.6 \pm 2.0	211.0 \pm 1.1

Note. Intensity ratios are reported with respect to $I(H\beta) = 100$, where the observed H β fluxes (in units of 10^{-16} erg s $^{-1}$ cm $^{-2}$) are reported in the second to last row. The color-excess values, $E(B - V)$, used to reddening correct the line ratios are listed in the last row.

associated with the measurement of the [S III] (λ 9069) line as we have discussed in Section 5.4.

Finally, we compare the SFR and EWs of H α and [O III] for each aperture, see panels (f)–(h) of Figure 12. Although, we find small changes in the inferred SFRs at a given aperture size, note that for apertures smaller than 1.5 we obtained slightly lower values of SFR for J0021+0052, J1044+0353, and J1418+2102. Moreover, the SFR and EWs converge when the aperture size is $\geq 5''$. We find high values of EWs for H α and [O III] for those galaxies, with an excellent agreement with those results derived from the SDSS spectra. We also note that the EWs of H α and [O III] of J0021+0052 show a drop in spectra with an aperture size of 1'' (due to the scale of panels (g) and (h) in Figure 12, such a structure is not visible) followed by an increase of the EW at an aperture of 1''.5. Such

behavior might be related to the complex structure in the core of J0021+0052.

6. Summary and Conclusions

A key goal of the CLASSY sample is to provide a unified picture of the stars and gas within nearby star-forming galaxies, which is largely derived from their FUV spectra. However, optical spectra that are well matched to the FUV spectra are also needed to derive a number of important nebular properties. We, therefore, analyzed the impact of aperture differences on the determination of nebular properties of 12 local star-forming galaxies at $z < 0.098$ for the CLASSY sample. This sample was chosen to have multiple optical spectra, including circular aperture, long-slit, and IFU spectroscopy. Specifically, we investigated the nebular properties of reddening, electron density and temperature, metallicities, ionization, and nebular

to stellar emission as probed by the $H\alpha$ and $[O\ III] \lambda 5007$ EW. In principle, the $3''$ diameter SDSS aperture is expected to cover most of the emission of CLASSY galaxies and is well matched to the FUV spectra observed with the HST/COS $2''.5$ aperture. Therefore, we use the SDSS spectra as the base of our comparison for the other optical spectra. Additionally, the IFU spectra allow us to inspect how the derived properties change as a function of aperture-extraction size, while eliminating any instrument effects. We summarize our main conclusions as follows.

1. We have calculated the reddening using three different Balmer ratios ($H\alpha/H\beta$, $H\gamma/H\beta$, and $H\delta/H\beta$) and found that the error-weighted average $E(B - V)$ value was insensitive to the aperture size of different spectra for our sample, with a median difference of less than 0.1 dex.

However, using the IFU observations of three CLASSY galaxies, we find that the $E(B - V)$ values derived from individual Balmer line ratios decrease (by up to 53%) with increasing aperture size, with the most significant change occurring in the center of the galaxies.

2. We calculated electron densities $[S\ II] \lambda\lambda 6717, 6731$ and temperatures from multiple auroral lines and found them to be insensitive to aperture size for our sample. In particular, investigating a range of aperture-extraction sizes from the IFU observations, we find that values change most significantly in the center of the galaxies, and level out near the COS aperture radius of $2''.5$. Similar results were found for reddening and metallicity.
3. We find a good agreement between the metallicities derived using the various aperture spectra for the same galaxy, with differences of <0.1 dex. Such small differences imply that the metallicity calculated from the optical spectra is representative of the region sampled in the FUV with COS for our CLASSY sample of the star-forming galaxies.

To summarize, we find that the aperture effects on inferred nebular properties are minimal for the CLASSY sample of star-forming galaxies. Here, we want to stress that despite the specific instrumental effects imprinted on the spectra, we find quite similar results. These results demonstrate the appropriateness of comparing the physical properties obtained in the optical for compact, highly star-forming galaxies with those using the $2''.5$ aperture of HST/COS (M. Mingozi et al. in preparation).

The CLASSY team thanks the referee for thoughtful feedback that improved the paper. K.Z.A-C and D.A.B. are grateful for the support for this program, HST-GO-15840, which was provided by NASA through a grant from the Space Telescope Science Institute, which is operated by the Association of Universities for Research in Astronomy, Incorporated, under NASA contract NAS5-26555. The CLASSY Collaboration extends special gratitude to the Lorentz Center for useful discussions during the "Characterizing Galaxies with Spectroscopy with a view for JWST" 2017 workshop that led to the formation of the CLASSY Collaboration and survey. The CLASSY Collaboration thanks the COS team for all their assistance and advice in the reduction of the COS data. K.Z.A-C also thanks Noah Rogers for helping with the MODS data reduction for the LBT spectra and Víctor Patiño-Álvarez and Héctor Ibarra-Medel for their helpful discussions on the use of the STARLIGHT code. B.L.J. is thankful for the support from the

European Space Agency (ESA). J.B. acknowledges the support of Fundação para a Ciência e a Tecnologia (FCT) through the research grants UIDB/04434/2020 and UIDP/04434/2020, through work contract No. 2020.03379.CEECIND, and through FCT project PTDC/FISAST/4862/2020. R.A. acknowledges the support of ANID Fondecyt Regular 1202007.

This work also uses observations obtained with the Large 11 Binocular Telescope (LBT). LBT is an international collaboration among institutions in the United States, Italy, and Germany. LBT's collaborative partners are The University of Arizona on behalf of the Arizona Board of Regents; Istituto Nazionale di Astrofisica, Italy; LBT Beteiligungsgesellschaft, Germany, representing the Max-Planck Society, The Leibniz Institute for Astrophysics Potsdam, and Heidelberg University; The Ohio State University, University of Notre Dame, University of Minnesota, and University of Virginia.

The STARLIGHT project is supported by the Brazilian agencies CNPq, CAPES, and FAPESP and by the France-Brazil CAPES/Cofecub program. Funding for SDSS-III has been provided by the Alfred P. Sloan Foundation, the Participating Institutions, the National Science Foundation, and the U.S. Department of Energy Office of Science.

The SDSS-III website is at <http://www.sdss3.org/>. SDSS-III is managed by the Astrophysical Research Consortium for the Participating Institutions of the SDSS-III Collaboration including the University of Arizona, the Brazilian Participation Group, Brookhaven National Laboratory, Carnegie Mellon University, University of Florida, the French Participation Group, the German Participation Group, Harvard University, the Instituto de Astrofísica de Canarias, the Michigan State/Notre Dame/JINA Participation Group, Johns Hopkins University, Lawrence Berkeley National Laboratory, Max Planck Institute for Astrophysics, Max Planck Institute for Extraterrestrial Physics, New Mexico State University, New York University, Ohio State University, Pennsylvania State University, University of Portsmouth, Princeton University, the Spanish Participation Group, University of Tokyo, University of Utah, Vanderbilt University, University of Virginia, University of Washington, and Yale University.

This work also uses the services of the ESO Science Archive Facility, observations collected at the European Southern Observatory under ESO programs 096.B-0690, 0103.B-0531, 0103.D-0705, and 0104.D-0503.

Appendix A Emission Line Intensities

1. Table 9: Emission line intensities measured for the APO/SDSS sample of 12 star-forming galaxies.
2. Table 10: Emission line intensities measured for the Keck/ESI sample of six star-forming galaxies.
3. Table 11: Emission line intensities measured for the VLT/MUSE sample of three star-forming galaxies.

ORCID iDs

Karla Z. Arellano-Córdova  <https://orcid.org/0000-0002-2644-3518>

Matilde Mingozi  <https://orcid.org/0000-0003-2589-762X>

Danielle A. Berg  <https://orcid.org/0000-0002-4153-053X>
 Bethan L. James  <https://orcid.org/0000-0003-4372-2006>
 Noah S. J. Rogers  <https://orcid.org/0000-0002-0361-8223>
 Alessandra Aloisi  <https://orcid.org/0000-0003-4137-882X>
 Ricardo O. Amorín  <https://orcid.org/0000-0001-5758-1000>
 Stéphane Charlot  <https://orcid.org/0000-0003-3458-2275>
 John Chisholm  <https://orcid.org/0000-0002-0302-2577>
 Timothy Heckman  <https://orcid.org/0000-0001-6670-6370>
 Matthew Hayes  <https://orcid.org/0000-0001-8587-218X>
 Svea Hernandez  <https://orcid.org/0000-0003-4857-8699>
 Tucker Jones  <https://orcid.org/0000-0001-5860-3419>
 Claus Leitherer  <https://orcid.org/0000-0003-2685-4488>
 Crystal L. Martin  <https://orcid.org/0000-0001-9189-7818>
 Themiya Nanayakkara  <https://orcid.org/0000-0003-2804-0648>
 Richard W. Pogge  <https://orcid.org/0000-0003-1435-3053>
 Ryan Sanders  <https://orcid.org/0000-0003-4792-9119>
 Peter Senchyna  <https://orcid.org/0000-0002-9132-6561>
 Evan D. Skillman  <https://orcid.org/0000-0003-0605-8732>
 Aida Wofford  <https://orcid.org/0000-0001-8289-3428>
 Xinfeng Xu  <https://orcid.org/0000-0002-9217-7051>

References

- Aggarwal, K. M., & Keenan, F. P. 1999, *ApJS*, **123**, 311
 Arellano-Córdova, K. Z., Esteban, C., García-Rojas, J., & Méndez-Delgado, J. E. 2020, *MNRAS*, **496**, 1051
 Arellano-Córdova, K. Z., & Rodríguez, M. 2020, *MNRAS*, **497**, 672
 Aver, E., Berg, D. A., Olive, K. A., et al. 2021, *JCAP*, **2021**, 027
 Berg, D. A., Chisholm, J., Erb, D. K., et al. 2021, *ApJ*, **922**, 170
 Berg, D. A., Erb, D. K., Henry, R. B. C., Skillman, E. D., & McQuinn, K. B. W. 2019, *ApJ*, **874**, 93
 Berg, D. A., James, B. L., King, T., et al. 2022, *ApJS*, **261**, 31
 Berg, D. A., Pogge, R. W., Skillman, E. D., et al. 2020, *ApJ*, **893**, 96
 Berg, D. A., Skillman, E. D., Croxall, K., et al. 2015, *ApJ*, **806**, 16
 Berg, D. A., Skillman, E. D., Garnett, D. R., et al. 2013, *ApJ*, **775**, 128
 Berg, D. A., Skillman, E. D., Henry, R. B. C., Erb, D. K., & Carigi, L. 2016, *ApJ*, **827**, 126
 Berg, D. A., Skillman, E. D., Marble, A., et al. 2012, *ApJ*, **754**, 98
 Brinchmann, J., Charlot, S., White, S. D. M., et al. 2004, *MNRAS*, **351**, 1151
 Bruzual, G., & Charlot, S. 2003, *MNRAS*, **344**, 1000
 Campbell, A., Terlevich, R., & Melnick, J. 1986, *MNRAS*, **223**, 811
 Cardelli, J. A., Clayton, G. C., & Mathis, J. S. 1989, *ApJ*, **345**, 245
 Chabrier, G. 2003, *PASP*, **115**, 763
 Cid Fernandes, R., Mateus, A., Sodré, L., Stasińska, G., & Gomes, J. M. 2005, *MNRAS*, **358**, 363
 Croxall, K. V., Pogge, R. W., Berg, D. A., Skillman, E. D., & Moustakas, J. 2016, *ApJ*, **830**, 4
 Curti, M., Cresci, G., Mannucci, F., et al. 2017, *MNRAS*, **465**, 1384
 De Robertis, M. M., Dufour, R. J., & Hunt, R. W. 1987, *JRASC*, **81**, 195
 Eisenstein, D. J., Weinberg, D. H., Agol, E., et al. 2011, *AJ*, **142**, 72
 Filippenko, A. V. 1982, *PASP*, **94**, 715
 Froese Fischer, C., & Tachiev, G. 2004, *ADNDT*, **87**, 1
 Garnett, D. R. 1992, *AJ*, **103**, 1330
 Gómez, P. L., Nichol, R. C., Miller, C. J., et al. 2003, *ApJ*, **584**, 210
 Green, G. M., Schlafly, E. F., Finkbeiner, D. P., et al. 2015, *ApJ*, **810**, 25
 Groves, B., Brinchmann, J., & Walcher, C. J. 2012, *MNRAS*, **419**, 1402
 Guseva, N. G., Izotov, Y. I., Fricke, K. J., & Henkel, C. 2017, *A&A*, **599**, A65
 Hill, J. M., Green, R. F., Ashby, D. S., et al. 2010, *Proc. SPIE*, **7733**, 77330C
 Hopkins, A. M., Miller, C. J., Nichol, R. C., et al. 2003, *ApJ*, **599**, 971
 Hudson, C. E., Ramsbottom, C. A., & Scott, M. P. 2012, *ApJ*, **750**, 65
 Izotov, Y. I., Stasińska, G., Meynet, G., Guseva, N. G., & Thuan, T. X. 2006, *A&A*, **448**, 955
 Izotov, Y. I., & Thuan, T. X. 1999, *ApJ*, **511**, 639
 James, B. L., Berg, D. A., King, T., et al. 2022, *ApJS*, in press, arXiv:2206.01224
 James, B. L., Kaposov, S. E., Stark, D. P., et al. 2017, *MNRAS*, **465**, 3977
 Kennicutt, R. C., & Evans, N. J. 2012, *ARA&A*, **50**, 531
 Kewley, L. J., Jansen, R. A., & Geller, M. J. 2005, *PASP*, **117**, 227
 Kisieliński, R., Storey, P. J., Ferland, G. J., & Keenan, F. P. 2009, *MNRAS*, **397**, 903
 Kobulnicky, H. A., Kennicutt, J. C. R., & Pizagno, J. L. 1999, *ApJ*, **514**, 544
 Kunth, D., & Östlin, G. 2000, *A&ARv*, **10**, 1
 Lequeux, J., Peimbert, M., Rayo, J. F., Serrano, A., & Torres-Peimbert, S. 1979, *A&A*, **80**, 155
 Luridiana, V., Morisset, C., & Shaw, R. A. 2015, *A&A*, **573**, A42
 Mannucci, F., Belfiore, F., Curti, M., et al. 2021, *MNRAS*, **508**, 1582
 McQuinn, K. B. W., Berg, D. A., Skillman, E. D., et al. 2020, *ApJ*, **891**, 181
 Méndez-Delgado, J. E., Esteban, C., García-Rojas, J., et al. 2021, *MNRAS*, **502**, 1703
 Mingozzi, M., Belfiore, F., Cresci, G., et al. 2020, *A&A*, **636**, A42
 Moustakas, J., & Kennicutt, R. C., Jr+ 2006, *ApJS*, **164**, 81
 Nakamura, O., Fukugita, M., Brinkmann, J., & Schneider, D. P. 2004, *AJ*, **127**, 2511
 Osterbrock, D. E. 1989, *Astrophysics of Gaseous Nebulae and Active Galactic Nuclei* (Mill Valley, CA: Univ. Science Books)
 Osterbrock, D. E., & Ferland, G. J. 2006, *Astrophysics of Gaseous Nebulae and Active Galactic Nuclei* (Mill Valley, CA: Univ. Science Books)
 Pagel, B. E. J., Simonson, E. A., Terlevich, R. J., & Edmunds, M. G. 1992, *MNRAS*, **255**, 325
 Pérez-González, P. G., Zamorano, J., Gallego, J., Aragón-Salamanca, A., & Gil de Paz, A. 2003, *ApJ*, **591**, 827
 Pérez-Montero, E., Hägele, G. F., Contini, T., & Díaz, Á. I. 2007, *MNRAS*, **381**, 125
 Podobedova, L. I., Kelleher, D. E., & Wiese, W. L. 2009, *JPCRD*, **38**, 171
 Pogge, R. W., Atwood, B., Brewer, D. F., et al. 2010, *Proc. SPIE*, **7735**, 77350A
 Reddy, N. A., Steidel, C. C., Pettini, M., Bogosavljević, M., & Shapley, A. E. 2016, *ApJ*, **828**, 108
 Rogers, N. S. J., Skillman, E. D., Pogge, R. W., et al. 2021, *ApJ*, **915**, 21
 Sánchez Almeida, J., Pérez-Montero, E., Morales-Luis, A. B., et al. 2016, *ApJ*, **819**, 110
 Scarlata, C., Colbert, J., Teplitz, H. I., et al. 2009, *ApJL*, **704**, L98
 Senchyna, P., Stark, D. P., Chevillard, J., et al. 2019, *MNRAS*, **488**, 3492
 Senchyna, P., Stark, D. P., Vidal-García, A., et al. 2017, *MNRAS*, **472**, 2608
 Shivaee, I., Reddy, N., Rieke, G., et al. 2020, *ApJ*, **899**, 117
 Skillman, E. D., Kennicutt, R. C., & Hodge, P. W. 1989, *ApJ*, **347**, 875
 Stasińska, G. 2005, *A&A*, **434**, 507
 Stevenson, C. C. 1994, *MNRAS*, **267**, 904
 Tayal, S. S. 2011, *ApJS*, **195**, 12
 Vilchez, J. M. 1995, *AJ*, **110**, 1090
 Zaritsky, D., Zabludoff, A. I., & Willick, J. A. 1995, *AJ*, **110**, 1602
 Zurita, A., Florido, E., Bresolin, F., Pérez-Montero, E., & Pérez, I. 2021, *MNRAS*, **500**, 2359